

Chemical evolution in the environment of intermediate mass young stellar objects:

NGC 7129 – FIRS 2 and LkH α 234

A. Fuente¹, J.R. Rizzo^{1,2}, P. Caselli³, R. Bachiller¹, and C. Henkel⁴

¹ Observatorio Astronómico Nacional (IGN), Campus Universitario, Apdo. 112, E-28800 Alcalá de Henares (Madrid), Spain

² Departamento de Física, Universidad Europea de Madrid, Urb. El Bosque, E-28670 Villaviciosa de Odón, Spain

³ Osservatorio Astrofisico di Arcetri, Largo Enrico Fermi 5, 50125 Firenze, Italy

⁴ Max-Planck-Institut für Radioastronomie, Auf dem Hügel 69, 53121 Bonn, Germany

the date of receipt and acceptance should be inserted later

Abstract. We have carried out a molecular survey of the Class 0 IM protostar NGC 7129 – FIRS 2 (hereafter FIRS 2) and the Herbig Be star LkH α 234 with the aim of studying the chemical evolution of the envelopes of intermediate-mass (IM) young stellar objects (YSOs). Both objects have similar luminosities ($\sim 500 L_{\odot}$) and are located in the same molecular cloud which minimizes the chemical differences due to different stellar masses or initial cloud conditions. Moreover, since they are located at the same distance, we have the same spatial resolution in both objects. A total of 17 molecular species (including rarer isotopes) have been observed in both objects and the structure of their envelopes and outflows is determined with unprecedented detail.

Our results show that the protostellar envelopes are dispersed and warmed up during the evolution to become a pre-main sequence star. In fact, the envelope mass decreases by a factor >5 from FIRS 2 to LkH α 234, while the kinetic temperature increases from ~ 13 K to 28 K. On the other hand, there is no molecular outflow associated with LkH α 234. The molecular outflow seems to stop before the star becomes visible.

These physical changes strongly affect the chemistry of their envelopes. The N₂H⁺ and NH₃ abundances seem to be quite similar in both objects. However, the H¹³CO⁺ abundance is a factor of ~ 3 lower in the densest part of FIRS 2 than in LkH α 234, very likely because of depletion. In contrast, the SiO abundance is larger by a factor of ~ 100 in FIRS 2 than in LkH α 234. CS presents a complex behavior since its emission arises in different envelope components (outflow, cold envelope, hot core) and could also suffer from depletion. The CH₃OH and H₂CO column densities are very similar in FIRS 2 and LkH α 234 which implies that the beam averaged abundances are a factor >5 larger in LkH α 234 than in FIRS 2. The same case is found for the PDR tracers CN and HCN which have similar column densities in both objects. Finally, a complex behavior is found for the deuterated compounds. While the DCO⁺/H¹³CO⁺ ratio decreases by a factor of ~ 4 from FIRS 2 to LkH α 234, the D₂CO/H₂CO ratios is within a factor 1.5 in both objects. The detection of a warm CH₃CN component with $T_k > 63$ K shows the existence of a hot core in FIRS 2. Thus far, only a handful of hot cores have been detected in low and intermediate mass stars.

Based on our results in FIRS 2 and LkH α 234, we propose some abundance ratios that can be used as chemical clocks for the envelopes of IM YSOs. The SiO/CS, CN/N₂H⁺, HCN/N₂H⁺, DCO⁺/HCO⁺ and D₂CO/DCO⁺ ratios are good diagnostics of the protostellar evolutionary stage.

Key words. Stars: formation – pre-main sequence – individual: LkH α 234 – ISM: abundances – clouds – individual: NGC 7129

1. Introduction

Chemistry is a powerful tool to study young stellar objects (YSOs) and their environments. On the one hand, chemistry is a diagnostic tool of the different envelope components. On the other hand, it is a good time indicator

during the protostellar evolution. Chemical studies have been used to determine the physical structure of low-mass YSOs (e.g. Maret et al. 2004; Jørgensen et al. 2004a,b). These studies have revealed, for example, the presence of warm regions where the ices evaporate giving rise to regions similar to hot cores in massive protostars. However, the chemistry of the two classes of objects is different

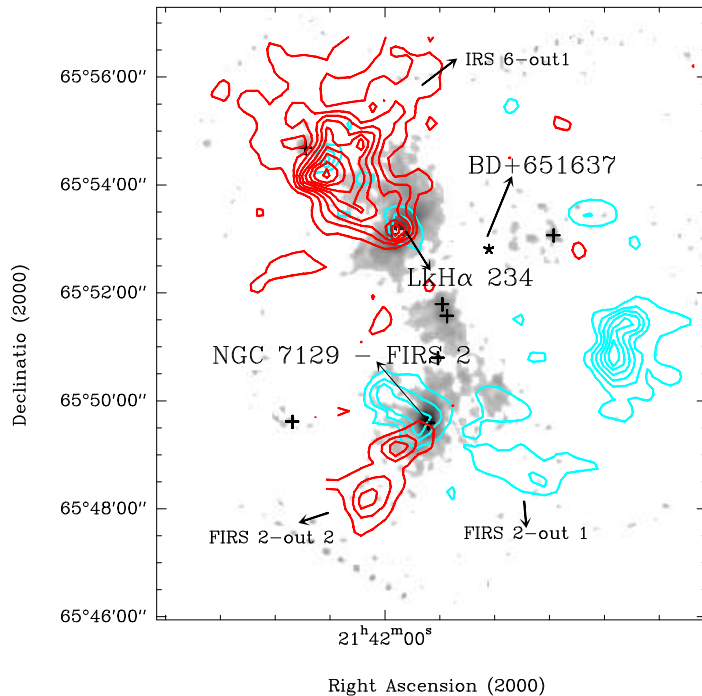


Fig. 1. Map of the 1.3mm continuum flux toward NGC 7129. Levels are 22.3, 44.6, 89.2, 178.4 to 713.6 mJy/beam by 178.4 mJy/beam. Crosses indicate the millimeter sources and stars the infrared sources. The red and blue contours represent the redshifted and blueshifted high-velocity gas of the nebula as traced by the ^{12}CO $J=2\rightarrow 1$ line. Velocity intervals are $[-30,-13]$ km s^{-1} for the blue lobe (grey contours) and $[-7,11]$ km s^{-1} for the red-lobe (dark contours). Contours are 10 to 60 K km s^{-1} in steps of 10 K km s^{-1} for the blue lobe and 10 to 100 K km s^{-1} in steps of 15 K km s^{-1} for the red lobe.

and rises questions on the mechanisms that lead to the observed chemical complexity and its dependence on the stellar mass (Cazaux et al. 2003; Bottinelli et al. 2004).

Chemistry has also been used as a time evolution indicator in both low-mass and high-mass objects. For instance, Maret et al. (2004) studied a sample of low-mass Class 0 objects and found some indications that the H_2CO abundance increases during the protostellar evolution. However, the different abundances can be due to different initial cloud conditions from which the protostars evolved. Further chemical studies are required to clarify this subject.

In this paper, we present a chemical study of the two intermediate mass (IM) YSOs, FIRS 2 and LkH α 234. Contrary to low-mass protostars, IM YSOs have been very little studied thus far, specially young protostars. For example, out of 42 Class 0 sources compiled by André et al. (2000), only six had luminosities in excess of $40 L_{\odot}$ (the precursors to HAe stars) and only one had a luminosity of $\sim 10^3 L_{\odot}$ (the precursor to HBe stars). IM YSOs ($M_{\star} \sim 2-10 M_{\odot}$) are not only an important link between low

mass and high mass stars but they share many characteristics of high mass star formation (clustering, PDR/HII regions) without the disadvantage of being too distant ($d \lesssim 1$ Kpc), or too complex. They are also important for the understanding of planet formation since Herbig Ae stars are the precursors of Vega-type systems. On a larger scale, they dominate the mean UV interstellar field in our Galaxy (Wolfire et al. 2003).

2. Target selection and observational strategy

FIRS 2 has been classified as a Class 0 IM object (Eiroa et al. 1998) and is, very likely, the youngest IM object known at present. An energetic bipolar molecular outflow is associated with it (Fuente et al. 2001). LkH α 234 is a embedded HBe star which still keeps a massive envelope ($M \sim 16 M_{\odot}$) but no bipolar molecular outflow seems to be driven by it (Fuente et al. 2001, 2002). These objects have the peculiarity of having similar luminosities ($\sim 500 L_{\odot}$) and be located in the same molecular cloud. During the protostellar and pre-main sequence evolution,

the luminosity remains quite constant for a given stellar mass (André et al. 2000). Thus, the same luminosity implies similar stellar mass. In addition, both sources are located in the same molecular cloud. This minimizes chemical effects due to very different stellar mass (both of them have $M_* \sim 5 M_\odot$) and/or different initial cloud conditions. Thus, in spite of our reduced sample, we have an excellent opportunity to find an evolutionary track for IM YSOs. In Fig. 1 we show the 1.3mm continuum map of the reflection nebula NGC 7129. Both, FIRS 2 (NGC 7129–FIRS 2) and LkH α 234 (NGC 7129 – FIRS 1) are associated with intense centrally peaked 1.3mm continuum and far infrared sources. We have also overlaid the red and blue lobes (as traced by the ^{12}CO J=2 \rightarrow 1 line) of the bipolar outflows associated to these YSOs (see Fuente et al. 2001 for a more detailed description). Clustering becomes significant in this range of stellar masses (Testi et al. 1999). Interferometric observations towards LkH α 234 show the existence of a young infrared companion (IRS 6) which is very likely the exciting source of the bipolar molecular outflow and the [SII] jet detected by Ray et al. (1990). The quadrupolar morphology of the outflow detected in NGC 7129–FIRS 2 is also due to the superposition of two bipolar molecular outflows FIRS 2-out 1 and FIRS 2-out 2 (Fuente et al. 2001). Fuente et al. (2001) proposed that FIRS 2-out 1 is associated with the Class 0 protostar while FIRS 2-out 2 is more likely associated with a more evolved infrared star (FIRS 2 - IR).

A complex chemical evolution occurred in the YSO envelopes during the protostellar evolution. This involves accretion of species in an icy mantle during the pre-collapse phase, followed by grain-surface chemistry and evaporation of ices once the YSO has started to heat its surroundings (e.g. Brown et al. 1988). In massive YSOs, the evaporated molecules drive a rapid high-temperature chemistry for a period of 10^4 – 10^5 years, resulting in the complex, saturated organic molecules ($\text{CH}_3\text{OCH}_3, \text{CH}_3\text{CN}, \text{C}_2\text{H}_5\text{OH}, \dots$), which are characteristic of a hot core (e.g. Charnley et al. 1992; Caselli et al. 1993; Rodgers & Charnley 2003; Nomura & Millar 2004; Viti et al. 2004). Once most of the envelope has been cleared up, the UV radiation can escape to form a photon-dominated-region (PDR) and, in the case of massive stars, an HII region. Simultaneously, the energetic bipolar outflows develop a shock chemistry in the surrounding molecular cloud.

To discern between the different envelope components and determine the protostellar envelope evolution, we have selected a set of molecular tracers. Specifically, NH_3 , N_2H^+ , H^{13}CO^+ and HC^{18}O^+ have been observed as tracers of the *cold envelope*; the volatile species CH_3OH and H_2CO to study the *warm envelope* where the icy grain mantles have been evaporated; the complex molecule CH_3CN to trace the *hot core*; and, CN and HCN in order to trace the incipient *PDR*. In addition, we have also observed several CS and C^{34}S lines that are useful to constrain the physical conditions of the envelope and SiO as an excellent tracer of the shock chemistry associated to

the *outflow*. The observation of the deuterated compounds $\text{N}_2\text{D}^+, \text{DCO}^+$ and D_2CO also provide us some information about how the deuterium fractionation is affected by the YSO evolution. Obviously, the “molecular tracer”–“envelope component” correspondence is not unique and all the species have contributions from other envelope components. Arguments based on the morphology of the emission, kinematics and different excitation conditions are used to discern between the different components in these cases.

3. Observations

The (J,K) = (1,1), (2,2), (3,3) and (4,4) inversion lines of ammonia were observed using the Effelsberg 100-m radiotelescope of the MPIFR in December 2000 and October 2002. We observed only one position in both sources. The half power beam width (HPBW) of the telescope at the rest frequency of the NH_3 lines, 23.7 GHz, was $40''$. We used the new cooled dual-channel HEMT K-band receiver with a typical system temperature of 200 K on a main beam brightness temperature scale. The 8192-channel autocorrelator was used as the backend. The four ammonia lines were observed simultaneously with a total bandwidth of 10 MHz and a channel separation of 0.098 km s^{-1} . We estimate that line intensities are accurate to within $\pm 15\%$.

The main set of observations were carried out with the IRAM 30m telescope in Pico de Veleta (Spain) during three different observing periods in May 1999, July 2002 and August 2003. The list of observed lines, the telescope characteristics at each frequency and a summary of the observations are shown in Table 1. When possible, all the lines of the same molecule were observed simultaneously in order to avoid observational errors. The backends were an autocorrelator split in several parts and a 256×100 kHz filter-bank. All the lines were observed with a spectral resolution of ~ 78 kHz except in the cases that are explicitly indicated in Table 1. The intensity scale used in this paper is main brightness temperature. Comparing the intensity of some pattern lines in different observing periods, we estimate that the calibration is accurate within a 20 % at 3mm and within a 30% at 1.3mm. We have observed a high S/N ratio spectra towards the star positions for all the lines listed in Table 1. In addition, we have carried out small maps in the most intense lines (see Table 1). In the case of the SiO 2 \rightarrow 1, SiO 3 \rightarrow 2, H^{13}CO^+ 1 \rightarrow 0 and CS 3 \rightarrow 2 lines we have mapped the entire outflows as traced by the high velocity CO emission. Fits to the observed lines at the (0,0) position are shown in Tables 2 and 3.

4. Analysis

The data have been analysed using the rotation diagram method. The molecular constants, the upper state energies and the partition functions required for applying this method have been taken from the JPL line catalog

Table 1. Description of the IRAM 30m observations

| Line | Freq. (GHz) | HPBW | η_{MB} | Observed positions |
|--|-----------------------|--------|-------------|---|
| N ₂ H ⁺ 1→0 | 93173.2 | 26.5'' | 0.71 | 60''×60'' map |
| CN 1→0 | 113490.0 | 23'' | 0.65 | 60''×60'' map (FIRS 2), 60''×100'' map (LkH α 234) |
| HCN 1→0 | 88631.8 | 27.5'' | 0.73 | 60''×60'' map (FIRS 2), 60''×100'' map (LkH α 234) |
| H ¹³ CO ⁺ 1→0 | 86754.3 | 27.5'' | 0.73 | complete map |
| HC ¹⁸ O ⁺ 1→0 | 85162.2 | 27.5'' | 0.73 | (0,0) |
| SiO 2→1 | 86846.9 | 27.5'' | 0.73 | complete map |
| SiO 3→2 | 130268.6 | 20'' | 0.60 | complete map |
| CS 3→2 | 146969.0 | 16.5'' | 0.55 | complete map |
| C ³⁴ S 2→1 | 96412.9 | 25.9'' | 0.70 | (0,0) |
| C ³⁴ S 3→2 | 144617.1 | 17'' | 0.55 | (0,0) |
| C ³⁴ S 5→4 | 192818.5 | 13'' | 0.47 | (0,0) |
| CH ₃ OH 2(1,3)→1(1,3) | 96755.5 | 26'' | 0.70 | 72''×72'' map |
| CH ₃ OH 2(0,3)→1(0,3) | 96744.6 | 26'' | 0.70 | 72''×72'' map |
| CH ₃ OH 2(1,4)→1(1,4) | 96741.4 | 26'' | 0.70 | 72''×72'' map |
| CH ₃ OH 2(0,1)→1(0,1) | 96739.4 | 26'' | 0.70 | 72''×72'' map |
| CH ₃ OH 3(0,3)→2(0,3) | 145093.7 | 17'' | 0.55 | (0,0) |
| CH ₃ OH 3(1,4)→2(1,4) | 145097.5 | 17'' | 0.55 | (0,0) |
| CH ₃ OH 3(0,1)→2(0,1) | 145103.2 | 17'' | 0.55 | (0,0) |
| CH ₃ OH 3(2,2)→2(2,2) ^a | 145124.4 | 17'' | 0.55 | (0,0) |
| CH ₃ OH 3(1,3)→2(1,3) | 145131.9 | 17'' | 0.55 | (0,0) |
| CH ₃ OH 5(2,4)→4(2,4) | 241904.1 | 10'' | 0.40 | 72''×72'' map |
| CH ₃ OH 5(0,1)→4(0,1) | 241791.4 | 10'' | 0.40 | 72''×72'' map |
| CH ₃ OH 5(1,4)→4(1,4) | 241767.2 | 10'' | 0.40 | 72''×72'' map |
| CH ₃ OH 5(3,1)→4(3,1) | 241832.9 ^a | 10'' | 0.40 | 72''×72'' map |
| CH ₃ OH 5(2,2)→4(2,2) | 241842.3 | 10'' | 0.40 | 72''×72'' map |
| CH ₃ OH 8(1,4)→7(0,3) | 229758.7 | 10.5'' | 0.42 | (0,0) |
| CH ₃ OH 11(1,4)→10(2,4) | 104300.5 | 24.5'' | 0.68 | (0,0) |
| H ₂ CO 3 ₁₂ →2 ₁₁ | 225697.8 | 10.5'' | 0.43 | 60''×60'' map (FIRS 2), 72''×72'' map (LkH α 234) |
| H ₂ CO 2 ₁₂ →1 ₁₁ | 140839.5 | 18'' | 0.57 | 60''×60'' map (FIRS 2), 72''×72'' map (LkH α 234) |
| H ₂ ¹³ CO 2 ₁₂ →1 ₁₁ | 137449.9 | 18'' | 0.57 | (0,0) |
| CH ₃ CN 5(0)→4(0) | 91987.0 | 27'' | 0.72 | (0,0) |
| CH ₃ CN 5(1)→4(1) | 91985.3 | 27'' | 0.72 | (0,0) |
| CH ₃ CN 5(2)→4(2) | 91980.0 | 27'' | 0.72 | (0,0) |
| CH ₃ CN 5(3)→4(3) | 91971.4 | 27'' | 0.72 | (0,0) |
| CN 2→1 | 226874.7 | 11'' | 0.42 | 60''×60'' map (FIRS 2), 60''×100'' (LkH α 234) |
| N ₂ D ⁺ 3→2 | 231321.7 | 10.5'' | 0.42 | (0,0) |
| DCO ⁺ 2→1 | 144077.3 | 17'' | 0.56 | 60''×60'' map |
| DCO ⁺ 3→2 | 216112.6 | 11'' | 0.44 | 60''×60'' map |
| D ₂ CO 4 ₀₄ →3 ₀₃ | 231410.3 | 10.5'' | 0.42 | (0,0) |

^a Only observed with a frequency resolution of 1 MHz.

(Pickett et al. 1998). This method gives the rotation temperature and total column density of a particular species knowing the integrated line intensities of several lines with different upper state energies. The rotation temperatures and column densities estimated in this way are shown in Table 4. The rotation temperature is a lower limit to the gas kinetic temperature, and only constitutes a good measure of the kinetic temperature if the lines are thermalized. This is the case of the ammonia inversion lines which are thermalized with densities, $n \sim 10^3 \text{ cm}^{-3}$. For this reason, we have used the NH₃ inversion lines to estimate the gas kinetic temperature of the different envelope components.

For some molecules we have only observed one transition. In this case we have calculated the total column density assuming optically thin emission, local thermodynamic equilibrium (LTE) and the rotation temperature

derived from a molecule with similar excitation requirements. In these cases we have marked with the superindex “a” the rotation temperature in Table 4.

The molecules NH₃, N₂H⁺, CN and HCN present hyperfine splitting. This allows us to derive the line opacity directly from the hyperfine line ratios. In these cases the column densities have been estimated directly from the line opacities. For N₂H⁺ and NH₃, we have also calculated the source size assuming the rotation temperature derived from the NH₃ inversion lines when the opacity of the main component is determined. We have made LVG calculation for SiO, CS and C³⁴S. These calculations are shown in Tables 6 and 8. In all the cases, we have fitted the densities assuming a fixed kinetic temperature. The assumed gas kinetic temperatures are based on those derived from the NH₃ data in Section 5.1 and are shown in

Table 2. Observational parameters towards NGC 7129 – FIRS 2

| Line | $T_{MB} \times \tau_m$ | V (km s $^{-1}$) | ΔV (km s $^{-1}$) | τ_m |
|---|--|---------------------|----------------------------|------------------|
| NH $_3$ (1,1) | 3.08(0.07) | -9.59(0.01) | 1.0(0.1) | 0.1 ^a |
| NH $_3$ (2,2) | 0.70(0.02) | -9.63(0.02) | 1.3(0.1) | 0.1 ^a |
| NH $_3$ (3,3) | 0.12(0.01) | -9.35(0.18) | 3.8(0.5) | 0.1 ^a |
| NH $_3$ (4,4) | rms = 0.05 K kms $^{-1}$ with $\Delta v=3.0$ kms $^{-1}$ | | | |
| N $_2$ H $^+$ 1 \rightarrow 0 | 9.22(0.02) | -9.51(0.01) | 1.91(0.01) | 1.28(0.10) |
| CN 1 \rightarrow 0 | 2.3(0.3) | -9.7(0.1) | 1.4(0.1) | 1.9 |
| HCN 1 \rightarrow 0 | 2.3(0.3) | -9.3(0.1) | 3.1(0.1) | 0.7 |
| Line | Area (K kms $^{-1}$) | V (km s $^{-1}$) | ΔV (km s $^{-1}$) | T_{MB} (K) |
| H 13 CO $^+$ 1 \rightarrow 0 | 1.92(0.02) | -9.74(0.01) | 1.27(0.02) | 1.39 |
| HC 18 O $^+$ 1 \rightarrow 0 | 0.17(0.02) | -9.68(0.09) | 1.1(0.2) | 0.14 |
| SiO 2 \rightarrow 1 | 1.55(0.09) | -7.5(0.2) | 6.8(0.4) | 0.21 |
| | 0.23(0.06) | -9.5(0.1) | 1.6(0.4) | 0.13 |
| SiO 3 \rightarrow 2 | 2.50(0.20) | -7.3(0.2) | 6.9(0.7) | 0.34 |
| CS 3 \rightarrow 2 | 3.69(0.12) | -9.1(0.1) | 5.81(0.24) | 0.60 |
| | 1.88(0.09) | -9.9(0.1) | 1.19(0.04) | 1.48 |
| C 34 S 2 \rightarrow 1 | 0.16(0.08) | -7.8(0.8) | 3.1(1.3) | 0.05 |
| | 0.28(0.07) | -9.8(0.1) | 1.3(0.2) | 0.20 |
| C 34 S 3 \rightarrow 2 | 1.05(0.08) | -9.4(0.1) | 4.3(0.4) | 0.23 |
| C 34 S 5 \rightarrow 4 | 1.21(0.16) | -8.8(0.3) | 4.2(0.7) | 0.27 |
| CH $_3$ OH 2(1,3) \rightarrow 1(1,3) | 0.6(0.3) | -9(1) | 5(3) | 0.11 |
| CH $_3$ OH 2(0,3) \rightarrow 1(0,3) | 1.85(0.06) | -8.20(0.09) | 6.1(0.2) | 0.28 |
| CH $_3$ OH 2(1,4) \rightarrow 1(1,4) | 4.71(0.05) | -9.2(0.2) | 3.0(0.2) | 1.47 |
| CH $_3$ OH 2(0,1) \rightarrow 1(0,1) | 5.83(0.07) | -9.58(0.01) | 5.3(0.1) | 1.03 |
| CH $_3$ OH 3(0,3) \rightarrow 2(0,3) | 4.12 (0.04) | -8.78(0.08) | 6.98(0.08) | 0.55 |
| CH $_3$ OH 3(1,4) \rightarrow 2(1,4) | 8.9(0.09) | -8.32(0.01) | 5.71(0.07) | 1.46 |
| CH $_3$ OH 3(0,1) \rightarrow 2(0,1) | 9.6(0.1) | -8.34(0.02) | 5.07(0.06) | 1.78 |
| CH $_3$ OH 3(2,2) \rightarrow 2(2,2) | 2(1) | -12(4) | 7(10) | 0.27 |
| CH $_3$ OH 3(1,3) \rightarrow 2(1,3) | 1.9(0.1) | -8.7(0.2) | 6.4(0.5) | 0.28 |
| CH $_3$ OH 5(2,4) \rightarrow 4(2,4) | 3(1) | -8.9(0.7) | 4(2) | 0.70 |
| CH $_3$ OH 5(0,1) \rightarrow 4(0,1) | 12.3(0.7) | -7.4(0.1) | 4.6(0.3) | 2.51 |
| CH $_3$ OH 5(1,4) \rightarrow 4(1,4) | 8.8(0.8) | -7.8(0.2) | 4.6(0.5) | 1.80 |
| CH $_3$ OH 5(3,1) \rightarrow 4(3,1) | 1.7(1.7) | -8.1(3) | 6.9(7) | 0.23 |
| CH $_3$ OH 5(2,2) \rightarrow 4(2,2) | 1.3(1.5) | -10(4) | 7(11) | 0.17 |
| CH $_3$ OH 8(1,4) \rightarrow 7(0,3) | 4.5(0.4) | -7.7(0.1) | 4.3(0.3) | 0.98 |
| CH $_3$ OH 11(1,4) \rightarrow 10(2,4) | 0.14(0.04) | -9.9(0.4) | 3.6(5.9) | 0.04 |
| H $_2$ CO 3 $_{12} \rightarrow$ 2 $_{11}$ | 2.3(0.2) | -9.6(0.1) | 1.3(0.1) | 1.66 |
| | 6.7(0.3) | -8.6(0.2) | 7.7(0.5) | 0.81 |
| H $_2$ CO 2 $_{12} \rightarrow$ 1 $_{11}$ | 3.0(0.1) | -9.66(0.01) | 1.41(0.03) | 2.00 |
| | 6.0(0.1) | -8.97(0.06) | 6.3(0.2) | 0.91 |
| H $_2$ 13 CO 2 $_{12} \rightarrow$ 1 $_{11}$ | 0.33(0.04) | -9.4(0.2) | 2.8(0.5) | 0.11 |
| CH $_3$ CN 5(0) \rightarrow 4(0) | 0.24(0.05) | -9.1(0.4) | 4.2(0.8) | 0.05 |
| CH $_3$ CN 5(1) \rightarrow 4(1) | 0.25(0.05) | -9.1(0.6) | 5(1) | 0.05 |
| CH $_3$ CN 5(2) \rightarrow 4(2) | 0.11(0.02) | -9.7(0.9) | 4(2) | 0.02 |
| CH $_3$ CN 5(3) \rightarrow 4(3) | 0.12(0.02) | -8(1) | 7(3) | 0.02 |
| CN 2 \rightarrow 1 | 2.74(0.24) | -9.7(0.1) | 2.6(0.2) | 1.0 |
| N $_2$ D $^+$ 3 \rightarrow 2 | 0.64(0.05) | -9.90(0.04) | 1.1(0.1) | 0.53 |
| DCO $^+$ 2 \rightarrow 1 | 2.93(0.04) | -9.86(0.01) | 1.0(0.1) | 2.61 |
| DCO $^+$ 3 \rightarrow 2 | 1.9(0.1) | -9.73(0.02) | 1.0(0.1) | 1.83 |
| D $_2$ CO 4 $_{04} \rightarrow$ 3 $_{03}$ | 0.3(0.1) | -9.6(0.3) | 3.9(1) | 0.05 |

^a In case of optically thin emission, τ_m cannot be determined and is set arbitrarily to 0.1.

Table 6 and 8. We have used the CS collisional coefficients calculated by Green & Chapman (1978) in the LVG calculations. The same collisional coefficients are used for SiO. This is a reasonable approximation since both molecules have the same mass and similar dipole moments. In the case of CS, we have been able to calculate the opacity and the source size because we have observed the main isotope and the rarer isotope C 34 S. All the column densities in Table 4, 6 and 8 are beam averaged column densities.

5. Results

5.1. NH $_3$

We have observed the ammonia (1,1), (2,2), (3,3) and (4,4) inversion transitions towards NGC 7129 – FIRS 2 and LkH α 234. All the spectra are shown in Fig. 1. The (1,1), (2,2) and (3,3) lines have been detected in both sources but only an upper limit has been obtained for

the (4,4) line. We have fitted these lines using the NH $_3$ procedure in the CLASS (this is the program dedicated to the analysis of single-dish spectra of the GILDAS softwares (<http://www.iram.fr/IRAMFR/GILDAS>)). This procedure fit all the hyperfine components assuming equal excitation temperature, central velocity and linewidth. The parameters given by the procedure are ($T_{ex} - T_{bg}$) $\times\tau_m$, V , ΔV , and τ_m where τ_m is the main group opacity and T_{ex} the excitation temperature (see Bachiller et al. 1987 for a more detailed description of this procedure). In case of optically thin emission τ_m cannot be determined and is set arbitrarily to 0.1.

The fits to the NH $_3$ lines in NGC 7129–FIRS 2 are shown in Table 2. The NH $_3$ emission is optically thin in all the lines. However, the linewidth of the (3,3) line is almost a factor of 3 larger than the linewidth of the (1,1) and (2,2) lines (see Table 2 and Fig. 2). In addition, the central velocity of the lines is slightly lower than those of the lower energy lines. This suggests that the (3,3) line is

Table 3. Observational parameters towards LkH α 234

| Line | $T_{MB} \times \tau_m$ | V (km s $^{-1}$) | ΔV (km s $^{-1}$) | τ_m |
|---|--|-------------------|----------------------------|------------------|
| NH $_3$ (1,1) | 0.60(0.03) | -9.87(0.02) | 0.9(0.2) | 0.86(0.07) |
| NH $_3$ (2,2) | 0.27(0.04) | -9.94(0.05) | 1.1(0.2) | 0.1 ^a |
| NH $_3$ (3,3) | 0.10(0.03) | -11(1) | 1.6(0.7) | 0.1 ^a |
| NH $_3$ (4,4) | rms = 0.13 K kms $^{-1}$ with $\Delta v=1.1$ kms $^{-1}$ | | | |
| N $_2$ H $^+$ 1 \rightarrow 0 | 1.53(0.06) | -9.48(0.01) | 1.82(0.04) | 1.32(0.7) |
| CN 1 \rightarrow 0 | 1.9(0.2) | -9.9(0.1) | 2.6(0.1) | 0.8 |
| HCN 1 \rightarrow 0 | 3.2(0.3) | -10.0(0.1) | 2.9(0.1) | 0.1 ^a |
| Line | Area (K kms $^{-1}$) | V (km s $^{-1}$) | ΔV (km s $^{-1}$) | T_{MB} (K) |
| H 13 CO $^+$ 1 \rightarrow 0 | 1.00(0.03) | -9.80(0.03) | 1.79(0.07) | 0.52 |
| HC 18 O $^+$ 1 \rightarrow 0 | 0.14(0.04) | -10.1(0.2) | 2(1) | 0.06 |
| SiO 2 \rightarrow 1 | 0.31(0.06) | -9.9(0.9) | 8.5(2.0) | 0.03 |
| SiO 3 \rightarrow 2 | 0.60(0.08) | -8.7(0.2) | 3.2(0.5) | 0.18 |
| CS 3 \rightarrow 2 | 14.9(0.2) | -9.7(0.1) | 3.0(0.1) | 4.67 |
| C 34 S 2 \rightarrow 1 | 0.66(0.04) | -9.9(0.1) | 3.4(0.2) | 0.18 |
| C 34 S 3 \rightarrow 2 | 1.41(0.05) | -9.5(0.1) | 3.2(0.2) | 0.41 |
| C 34 S 5 \rightarrow 4 | 1.71(0.22) | -9.1(0.3) | 4.5(0.8) | 0.36 |
| CH $_3$ OH 2(1,3) \rightarrow 1(1,3) | 0.3(0.1) | -7(3) | 12(5) | 0.02 |
| CH $_3$ OH 2(0,3) \rightarrow 1(0,3) | 0.20(0.04) | -9.8(0.3) | 2.9(0.7) | 0.06 |
| CH $_3$ OH 2(1,4) \rightarrow 1(1,4) | 0.48(0.03) | -9.6(0.1) | 2.2(0.2) | 0.20 |
| CH $_3$ OH 2(0,1) \rightarrow 1(0,1) | 0.64(0.04) | -9.5(0.1) | 5.2(0.4) | 0.11 |
| CH $_3$ OH 3(0,3) \rightarrow 2(0,3) | 1.27(0.09) | -9.5(0.1) | 4.6(0.4) | 0.26 |
| CH $_3$ OH 3(1,4) \rightarrow 2(1,4) | 1.91(0.09) | -9.2(0.1) | 4.8(0.3) | 0.37 |
| CH $_3$ OH 3(0,1) \rightarrow 2(0,1) | 1.94(0.07) | -9.2(0.1) | 3.3(0.2) | 0.55 |
| CH $_3$ OH 3(2,2) \rightarrow 2(2,2) | 1.6(0.4) | -12(1) | 9(4) | 0.17 |
| CH $_3$ OH 3(1,3) \rightarrow 2(1,3) | 1.3(0.4) | -10(1) | 8(3) | 0.15 |
| CH $_3$ OH 5(2,4) \rightarrow 4(2,4) | 2.6(0.5) | -9.4(0.5) | 5(1) | 0.49 |
| CH $_3$ OH 5(0,1) \rightarrow 4(0,1) | 2.9(0.2) | -8.8(0.1) | 4.1(0.6) | 0.66 |
| CH $_3$ OH 5(1,4) \rightarrow 4(1,4) | 2.1(0.2) | -9.2(0.1) | 3.1(0.2) | 0.64 |
| CH $_3$ OH 8(1,4) \rightarrow 7(0,3) | 2.0(0.3) | -9.7(0.5) | 7(1) | 0.27 |
| CH $_3$ OH 11(1,4) \rightarrow 10(2,4) | 0.13(0.04) | -9.9(0.8) | 6(2) | 0.02 |
| H $_2$ CO 3 $_{12}$ \rightarrow 2 $_{11}$ | 5.4(0.3) | -9.4(0.1) | 2.2(0.1) | 2.2 |
| | 5.9(0.3) | -9.8(0.1) | 5.5(0.2) | 1.0 |
| H $_2$ CO 2 $_{12}$ \rightarrow 1 $_{11}$ | 8.1(0.6) | -9.7(0.1) | 2.4(0.1) | 3.1 |
| | 3.1(0.6) | -9.5(0.2) | 6(1) | 0.5 |
| H $_2$ 13 CO 2 $_{12}$ \rightarrow 1 $_{11}$ | 0.24(0.05) | -9.4(0.4) | 4(1) | 0.05 |
| CH $_3$ CN 5(0) \rightarrow 4(0) | 0.17(0.02) | -10.2(0.2) | 2.6(0.4) | 0.06 |
| CH $_3$ CN 5(1) \rightarrow 4(1) | 0.16(0.02) | -9.9(0.2) | 2.9(0.4) | 0.05 |
| CH $_3$ CN 5(2) \rightarrow 4(2) | < 0.07 K kms $^{-1}$ with $\Delta v=3.2$ km s $^{-1}$ | | | |
| CH $_3$ CN 5(3) \rightarrow 4(3) | < 0.07 K kms $^{-1}$ with $\Delta v=3.2$ km s $^{-1}$ | | | |
| CN 2 \rightarrow 1 | 6.0(0.3) | -9.0(0.1) | 2.9(0.2) | 1.9 |
| N $_2$ D $^+$ 3 \rightarrow 2 | $\sigma=0.11$ K kms $^{-1}$ en $\Delta v=1.5$ km s $^{-1}$ | | | |
| DCO $^+$ 2 \rightarrow 1 | 0.62(0.04) | -9.58(0.04) | 1.5(0.1) | 0.38 |
| DCO $^+$ 3 \rightarrow 2 | 0.76(0.07) | -9.4(0.1) | 2.2(0.2) | 0.33 |
| D $_2$ CO 4 $_{04}$ \rightarrow 3 $_{03}$ | 0.60(0.2) | -9.1(0.5) | 4(1) | 0.15 |

^a In case of optically thin emission, τ_m cannot be determined and is set arbitrarily to 0.1.

arising in a different region than the (1,1) and (2,2) lines. This interpretation is reinforced by the NH $_3$ rotational diagram (see Fig. 3). The three lines detected in NGC 7129–FIRS 2 cannot be fitted by one single straight line which implies the existence of at least two gas components with different rotation temperatures, a cold component traced by the (1,1) and (2,2) lines and a hot component only detected with the (3,3) line. Using the (1,1) and (2,2) lines, we derive a rotation temperature, $T_{12}=13$ K and a column density, $N(\text{NH}_3)=4.9 \cdot 10^{14}$ cm $^{-2}$ for the cold component. Because of the lack of radiative transitions between different K-ladders, the ammonia inversion lines are good thermometers of dense clouds. In fact, detailed radiative transfer calculations for NH $_3$ show that $T_k=T_{12}$ for $T_k<20$ K (Danby et al. 1988). This low value of the kinetic temperature in the cold envelope implies that depletion could be important in this young protostar.

Since we have not detected the (4,4) line, we can only derive lower and upper limits for the rotation temperature of the hot component. The lower limit is given for the excitation temperature between the (1,1) and (3,3) lines, and the upper limit is given for the excitation temperature be-

tween the (3,3) line and the upper limit to the (4,4) line. We obtain that the hot component has a rotation temperature, $T_{rot}\sim 30-90$ K, which implies a lower limit of 50 K to the kinetic temperature of this component. We have estimated $N(\text{NH}_3)\sim 1.5 \cdot 10^{13}$ cm $^{-3}$ for the hot component. This value has been derived from the integrated intensity of the (3,3) line assuming $T_{rot}=90$ K and LTE conditions and is, in fact, a lower limit to the actual column density of the hot gas.

The same procedure has been repeated for the ammonia lines towards LkH α 234. Similarly to NGC 7129 – FIRS 2, the ammonia emission towards LkH α 234 cannot be fitted with one single rotation temperature (see Fig. 3). However, in this case the linewidth of the (3,3) line is more similar to those of the (1,1) and (2,2) lines (see Table 3). The linewidths seem to increase monotonically with the energy of the transition, but there is not a jump between the linewidth of the (3,3) line and those of the others as in the case of the protostar. We have fitted a two components model to the rotational diagram in LkH α 234 and obtained rotation temperatures of ~ 22 K and $\sim 49-134$ K for cold and hot components respectively. This implies

Table 4. LTE column densities

| NGC 7129 – FIRS 2 | | | | | LkH α 234 | | | | |
|-------------------|----------|---------------|--------------------------|---------------|-------------------|----------|-----------------------|--------------------------|------------|
| Molecule | Comp | T_{rot} (K) | N^b (cm $^{-2}$) | Ω_s | Molecule | Comp | T_{rot} (K) | N^b (cm $^{-2}$) | Ω_s |
| NH $_3$ | Cold | 13 | $4.9 \cdot 10^{14}$ | $\sim 21''$ | NH $_3$ | Cold | 22 | $4.0 \cdot 10^{13}$ | $8''$ |
| | Warm | 31 – 87 | $\sim 1.5 \cdot 10^{13}$ | | NH $_3$ | Warm | 49 – 134 | $\sim 1.1 \cdot 10^{13}$ | |
| N $_2$ H $^+$ | | 13^a | $3.8 \cdot 10^{13}$ | | N $_2$ H $^+$ | | 22^a | $1.0 \cdot 10^{13}$ | $\sim 8''$ |
| H 13 CO $^+$ | | 13^a | $2.2 \cdot 10^{12}$ | | H 13 CO $^+$ | | 22^a | $1.7 \cdot 10^{12}$ | |
| CH $_3$ OH | | 17 | $7.8 \cdot 10^{14}$ | | CH $_3$ OH p | | 24 | $1.4 \cdot 10^{14}$ | |
| | Hot core | >80 | $\sim 2.0 \cdot 10^{14}$ | | CH $_3$ OH e | | >250 | $\sim 4.0 \cdot 10^{14}$ | |
| | | | | | CH $_3$ OH e | | 59 | $4.8 \cdot 10^{14}$ | |
| H $_2$ CO | Narrow | ~ 10 | $2.2 \cdot 10^{13}$ | | H $_2$ CO | | ~ 11 | $8.0 \cdot 10^{13}$ | |
| | Wide | ~ 9 | $4.8 \cdot 10^{13}$ | | H $_2$ 13 CO | | $\sim 11^a$ | $2.4 \cdot 10^{12}$ | |
| H $_2$ 13 CO | | $\sim 10^a$ | $2.3 \cdot 10^{12}$ | | CH $_3$ CN | Hot core | <53 | $> 2.0 \cdot 10^{12b}$ | |
| CH $_3$ CN | | 63 | $3.6 \cdot 10^{12}$ | CN | | 6.5 | $6.1 \cdot 10^{13}$ | | |
| CN | | 5 | $4.8 \cdot 10^{13}$ | HCN | | 6.5^a | $2.1 \cdot 10^{13}$ | | |
| HCN | | 5^a | $1.6 \cdot 10^{13}$ | N $_2$ D $^+$ | | 22^a | $< 2.3 \cdot 10^{11}$ | | |
| N $_2$ D $^+$ | | 13^a | $5.4 \cdot 10^{11}$ | DCO $^+$ | | 17 | $4.2 \cdot 10^{11}$ | | |
| DCO $^+$ | | 8.5 | $1.8 \cdot 10^{12}$ | D $_2$ CO | | 11^a | $3.7 \cdot 10^{12}$ | | |
| D $_2$ CO | | 10^a | $2.0 \cdot 10^{12}$ | | | | | | |

^a Assumed rotation temperature.

^p Assuming a point source.

^e Assuming a beam filling factor of 1.

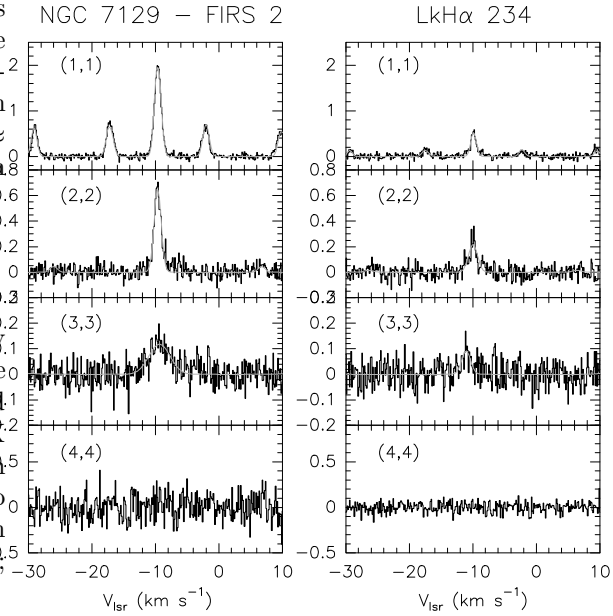
a kinetic temperature of $T_k \sim 28$ K for the cold envelope (Danby et al. 1988) and a lower limit of $T_k > 100$ K for the hot component. Contrary to FIRS 2, the (1,1) line is moderately thick in this source. This allows us to estimate the size of the NH $_3$ emission. Assuming that the excitation temperature of the (1,1) line is equal to the rotation temperature of the cold component, we obtain a size of $\approx 8''$, which is lower than the size of the clump in the 1.3mm continuum emission.

5.2. N $_2$ H $^+$, H 13 CO $^+$

Recent studies in pre-stellar cores reveal that the widely used tracers of dense gas, C 18 O and CS, are not adequate to trace dense cold clumps. Both are strongly depleted in the core at densities of a few 10^4 cm $^{-3}$ and $T_k < 20$ K (Tafalla et al. 2004). Only nitrogenated molecules seem to be unaffected by depletion. In fact, N $_2$ H $^+$ seems to keep a constant abundance through the core and is an excellent tracer of the cold gas (e.g. Caselli et al. 1999; Tafalla et al. 2002).

We have made small maps in the N $_2$ H $^+$ 1-0 and the H 13 CO $^+$ 1-0 lines toward FIRS 2 and LkH α 234. In addition we have observed the HC 18 O $^+$ line towards the star position to have an estimate of the opacity of the H 13 CO $^+$ 1-0 line. In Fig. 4 and 5 we show the N $_2$ H $^+$ 1-0 and the H 13 CO $^+$ 1-0 line integrated intensity maps together with the continuum map at 1.3mm, and in Table 2 and 3 we show the fits to the molecular lines. Due to the splitting of the N $_2$ H $^+$ 1 \rightarrow 0 line, we can have an estimate of the line opacity using the same method as in the case of NH $_3$.

Intense centrally-peaked emission is observed in the continuum map at 1.3mm toward FIRS 2. The same mor-


Fig. 2. Spectra of the NH $_3$ (1,1), (2,2), (3,3) and (4,4) inversion lines towards NGC 7129 – FIRS 2 (left) and LkH α 234 (right).

phology is observed in the H 13 CO $^+$ and N $_2$ H $^+$ maps, although the profile of the H 13 CO $^+$ emission is flatter than that of N $_2$ H $^+$. To quantify this difference in the emission profile, we have calculated the line intensity ratio, $r_1 = I_m(N_2H^+)/I(H^{13}CO^+)$, where $I_m(N_2H^+)$ is the inten-

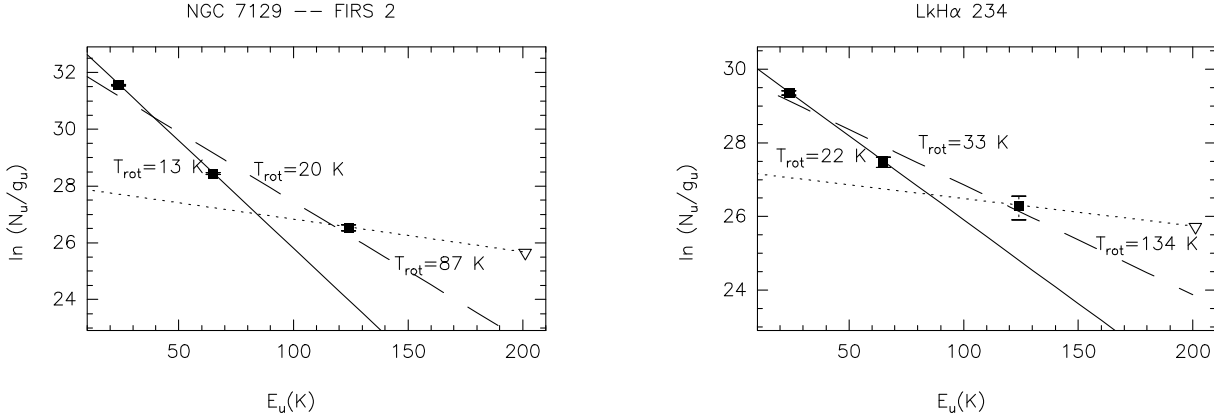


Fig. 3. Rotational diagram of NH_3 in NGC 7129 – FIRS 2 and LkH α 234. The long-dashed line corresponds to the fit assuming a single rotation temperature for all the transitions. The solid and dotted lines are the warm and cold component respectively of the two-components model.

sity of the main component of the N_2H^+ $1\rightarrow 0$ line and $I(\text{H}^{13}\text{CO}^+)$ the intensity of the H^{13}CO^+ $1\rightarrow 0$ line, in a radial strip at $0''$ offset in declination. The ratio r_1 changes from 2.7 at the center of the clump to 1.5 at an offset of $(-30'', 0'')$. Using the LTE approximation with $T_{\text{rot}} = 13$ K (based on our NH_3 calculations) and assuming optically thin emission in the H^{13}CO^+ line, we derive that the $\text{N}_2\text{H}^+/\text{H}^{13}\text{CO}^+$ abundance ratio changes from ~ 17 in the $(0,0)$ position to ~ 5 at $(-30'', 0)$. Thus, the abundance of H^{13}CO^+ relative to N_2H^+ seems to decrease by a factor of ~ 3 towards the clump center. However, this change in the estimated H^{13}CO^+ abundance could be due to the larger opacity of the H^{13}CO^+ line. To constrain the opacity of the H^{13}CO^+ $1\rightarrow 0$ line, we have observed the HC^{18}O^+ $1\rightarrow 0$ line towards the $(0,0)$ position. The H^{13}CO^+ $1\rightarrow 0$ / HC^{18}O^+ $1\rightarrow 0$ line intensity ratio is ~ 11 , showing that the H^{13}CO^+ $1\rightarrow 0$ line is optically thin at this position.

In the above calculations, we have assumed that the rotation temperature is uniform in all the strip. This assumption could be unrealistic since the density and kinetic temperature are expected to decrease with the distance from the star. We have used an LVG code to investigate if the different values of r_1 are due to a gradient in the physical conditions in the clump or/and are the result of a change in the relative abundance of both molecules. Since we are comparing the ground state lines of both species, the ratio r_1 is very little dependent on the kinetic temperature and depends mainly on the hydrogen density and the $\text{N}_2\text{H}^+/\text{H}^{13}\text{CO}^+$ abundance ratio. In Fig. 6 we show the ratio r_1 and the opacity of the main hyperfine N_2H^+ $1\rightarrow 0$ line for a wide range of physical conditions assuming $X = \text{N}_2\text{H}^+/\text{H}^{13}\text{CO}^+ = 3, 7, 15$. The values of the opacity and r_1 measured towards the star position can only be fitted assuming $X=15$ (see Fig. 6). A lower value of X would imply that the N_2H^+ line is optically thin in contradiction

with our observational results. On the contrary, the value measured at the offset $(-30'', 0'')$ can only be fitted with $X < 7$. Thus we conclude that the gradient in the value of r_1 cannot be due to the expected gradient in the excitation temperature of the observed lines across the clump, but to a gradient in the $\text{N}_2\text{H}^+/\text{H}^{13}\text{CO}^+$ abundance ratio.

As commented above, detailed studies in pre-stellar clumps show that the abundance of N_2H^+ remains constant in these cold clumps while H^{13}CO^+ could suffer from depletion in the densest part (Lee et al. 2003; Caselli et al. 2002). Assuming that N_2H^+ has a constant abundance in the clump, we need to assume an H^{13}CO^+ depletion factor ~ 2 to fit our observations.

The integrated intensity maps of the H^{13}CO^+ $1\rightarrow 0$ and N_2H^+ $1\rightarrow 0$ lines towards LkH α 234 are shown in Fig. 5. The N_2H^+ $1\rightarrow 0$ map presents a very different morphology to that of the continuum and the H^{13}CO^+ maps. While the continuum map presents a intense point-like emission at the position of LkH α 234, the N_2H^+ map peaks at the offset $(-6'', +18'')$. The map of the H^{13}CO^+ line show both peaks. As we will argue in the following, these different morphologies can only be explained if one assumes a different temperature and chemistry between both peaks.

In Table 4 we show the estimated N_2H^+ and H^{13}CO^+ column densities in LkH α 234 assuming a rotation temperature of 22 K derived from the NH_3 observations. We have obtained $N(\text{N}_2\text{H}^+) \sim 1.0 \cdot 10^{13} \text{ cm}^{-2}$ and a $\text{N}_2\text{H}^+/\text{H}^{13}\text{CO}^+$ abundance ratio of ~ 6 . The $\text{N}_2\text{H}^+/\text{H}^{13}\text{CO}^+$ ratio in LkH α 234 is lower than that found in FIRS 2.

We have repeated the same calculations for the offset $(-6'', +18'')$. Continuum observations suggests that this clump is colder than that associated to LkH α 234. In fact, if we assume that the N_2H^+ abundance is uniform in the region and a typical dust temperature of 30 K towards LkH α 234, we need to assume a dust temperature $\lesssim 10$ K

at the offset ($-6''$, $+18''$) in order to explain the measured continuum flux. Thus, we have assumed a rotation lower temperature, $T_{rot} \sim 10$ K, in our LTE calculations. With these assumptions, we obtain a N_2H^+ column density of $\sim 1.3 \cdot 10^{13} \text{ cm}^{-2}$ and a $N_2H^+/H^{13}CO^+$ abundance ratio of ~ 10 . This value is intermediate between those measured in LkH α 234 and FIRS 2. However, the difference is of a factor of 2 which is within the uncertainty involved in these kind of calculations. Based on our results, we can propose an evolutionary trend based on the $N_2H^+/H^{13}CO^+$ ratio. This ratio is maximum in the IM Class 0 object FIRS 2 where molecular depletion is significant, it may take an intermediate value in the infrared low-mass star IRS 6 and is minimum in the envelope of the more evolved object, the HBe star LkH α 234.

5.3. CO outflows, SiO

The SiO abundance is strongly enhanced (up to several orders of magnitude) in shocked regions. However, its abundance is very low in dark clouds and PDRs (Schilke et al. 2001). Because of this peculiarity, SiO is used as a diagnostic for shocks in both galactic and extragalactic regions (e.g. Bachiller et al. 1991; Martín-Pintado et al. 1992; García-Burillo et al. 2000, 2001). In particular, it is commonly used to look for the energetic outflows associated with the youngest stellar objects. We have carried out maps of the $J=2 \rightarrow 1$ and $3 \rightarrow 2$ rotational lines of SiO around FIRS 2 and LkH α 234 to study the physical conditions and chemistry of the bipolar outflows found in these regions.

Interferometric and single-dish CO $2 \rightarrow 1$ observations show the existence of two bipolar outflows associated with FIRS 2. The axis of these outflows form an angle of almost 90° giving a quadrupolar morphology to the spatial distribution of the high velocity gas of the region. In Fig. 7 we show the maps of the high velocity ^{12}CO $2 \rightarrow 1$ emission reported by Fuente et al. (2001). Interferometric observations shows that the NE-SW outflow, hereafter FIRS 2-out 1, is the one associated with the millimeter source FIRS 2-MM1. An intense blue lobe is detected in the CO $2 \rightarrow 1$ emission in this outflow while the red lobe is only marginally detected. The NW-SE outflow, hereafter FIRS 2-out 2, seems to be associated with an infrared star FIRS 2-IR (Fuente et al. 2001). In FIRS 2-out 2, the red lobe is more prominent than the blue one, giving a peculiar appearance to the high velocity gas around FIRS 2. The peaks of the ^{12}CO emission in this lobe present a “Z”-like shape which suggests that the axis of the outflow FIRS 2-out 2 is precessing. Precession has been found in bipolar outflows associated to young low-mass stars (Gueth et al. 1996).

In Fig. 8 we present the integrated intensity map of the SiO $2 \rightarrow 1$ line towards FIRS 2. The SiO emission is only observed along the axis of the two outflows. Furthermore the SiO peaks are not located at the star position but in the bow shocks located at the end of the outflow lobes. Thus,

the SiO emission seems to be closely related to the bipolar outflows. The spectra of the SiO lines towards some selected positions are shown in Fig. 8. The SiO $2 \rightarrow 1$ line towards the star position presents two velocity components, a narrow component with $\Delta v \sim 1.6 \text{ km s}^{-1}$ which is centered at the velocity of the ambient cloud, $V_{lsr} \sim -10.0 \text{ km s}^{-1}$, and a wide component, $\Delta v \sim 7.0 \text{ km s}^{-1}$ which is centered at $V_{lsr} \sim -7.0 \pm 1.0 \text{ km s}^{-1}$. The component at -7.0 km s^{-1} corresponds to a well defined high velocity clump which peaks at the position ($-10''$, $-10''$) (see Fig. 8). Hereafter we will refer to this clump as R1. There exists a counterpart blue clump at a velocity, $V_{lsr} \sim -12.5 \pm 0.5 \text{ km s}^{-1}$ which peaks at the position ($50''$, $50''$) (hereafter B1). At this position, the profile of the SiO $2 \rightarrow 1$ line only presents a wide component with $\Delta v \sim 7 \text{ km s}^{-1}$. The high velocity clumps R1 and B1 have well defined velocities and positions like the “bullets” found in low-mass stars (see Bachiller 1996). The jet-like morphology of the SiO emission along the outflow axis as well as the existence of bullets argues in favor of the youth of this outflow.

The component at the velocity of the ambient cloud, $V_{lsr} \sim -10.0 \text{ km s}^{-1}$, is also present in FIRS 2-out 2. The emission of this narrow component in FIRS 2-out 2 is surrounding the red lobe as detected in ^{12}CO . In fact, the narrow component is located adjacent to the peaks of the high velocity CO emission suggesting that SiO emission is tracing the molecular cloud gas entrained in the outflow. Narrow SiO components widespread in the molecular cloud in which the bipolar outflow is embedded has been detected in other Class 0 protostars (Codella et al. 1999). We propose an interpretation in which the morphology of the SiO emission is related to the evolutionary stage of the outflow. In FIRS 2-out 1, the SiO emission has a jet-like morphology and is concentrated in “bullets” ejected by the exciting star. This “jet-like” morphology is also observed in the interferometric ^{12}CO image reported by (Fuente et al. 2001). The SiO emission in FIRS 2-out 2 is surrounding the red CO lobe. We propose that in this case the SiO emission traces the material adjacent to the cavity walls excavated by the outflow which is being entrained into the outflow. The different profiles of the SiO emission in FIRS 2-out 1 and FIRS 2-out 2 are clearly seen in Fig. 8.

We have calculated the SiO $3 \rightarrow 2/2 \rightarrow 1$ line intensity ratio, r_{32} , at the ($0''$, $0''$) position by degrading the angular resolution of the SiO $3 \rightarrow 2$ map to that of the SiO $2 \rightarrow 1$ one. A value of $r_{32} \sim 0.8$ is found in the three channels centered at the ambient velocity, while a value $r_{32} > 1.0$ is found for the high velocity gas. This reveals a higher excitation temperature for the high velocity gas. In order to determine the physical conditions for both components, we have used an LVG code. Since r_{32} suggests different physical conditions for the different velocity ranges, we have carried out LVG calculations for the ambient, moderate velocity and high velocity gas components (see Table 6). Taking into account the kinetic temperature derived from the NH_3 lines we have assumed $T_k = 15$ K for the ambient narrow component and $T_k = 50$ K for

Table 5. Beam averaged N_2H^+ and H^{13}CO^+ column densities

| Source | T_{rot} (K) | $\text{N}(\text{H}^{13}\text{CO}^+)$ (cm^{-2}) | $\text{N}(\text{N}_2\text{H}^+)$ (cm^{-2}) | $\text{N}_2\text{H}^+/\text{H}^{13}\text{CO}^+$ |
|------------------|---------------|--|--|---|
| FIRS 2 | 13 | $2.2 \cdot 10^{12}$ | $3.8 \cdot 10^{13}$ | 17 |
| (-30,0) | 13 | $8.0 \cdot 10^{11}$ | $4.2 \cdot 10^{12}$ | 5 |
| LkH α 234 | 22 | $1.7 \cdot 10^{12}$ | $1.0 \cdot 10^{13}$ | 6 |
| (-6,+18) | 10 | $8.8 \cdot 10^{11}$ | $8.5 \cdot 10^{12}$ | ~ 10 |

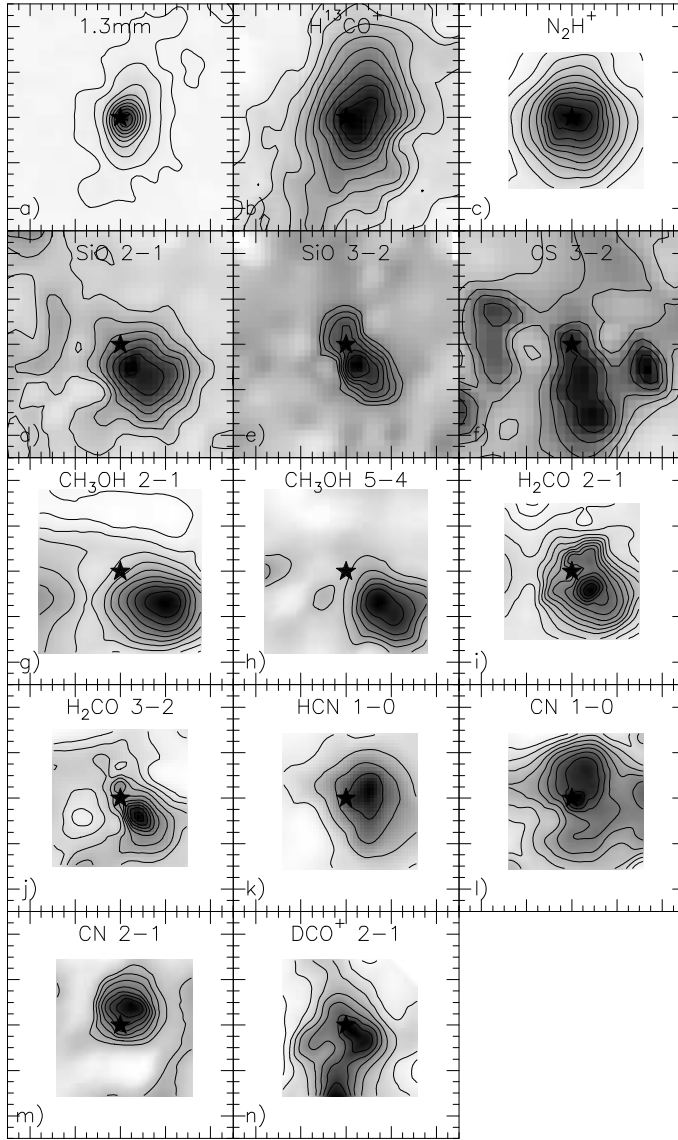


Fig. 4. Continuum map at 1.3mm and integrated intensity maps of the observed lines in NGC 7129 – FIRS 2. The box size is $100'' \times 100''$ and is centered at the star position. Contour levels are: a) 39.2 mJy/beam, and from 78.5 to 706.2 mJy/beam by 78.5 mJy /beam ;b) 0.19 to 1.7 by 0.19 K kms^{-1} ; c) 0.2 to 8.2 by 0.8 K kms^{-1} . d) 0.25 to 4 by 0.5 K kms^{-1} ; e) 1.5 to 4 by 0.5 K kms^{-1} ; f) 1.5 to 13.5 by 1.0 K kms^{-1} ; g) 2 to 20 by 2 K kms^{-1} ; h) 0.1 to 0.5 by 0.1 K kms^{-1} ; i) 1 to 14 by 1 K kms^{-1} ; j) 1 to 21 by 2 K kms^{-1} ; k) 2 to 7 by 1 K kms^{-1} ; l) 0.2 to 1.9 by 0.2 K kms^{-1} ; m) 0.8 to 3.4 by 0.4 K kms^{-1} ; n) 0.2 to 3 by 0.4 K kms^{-1} .

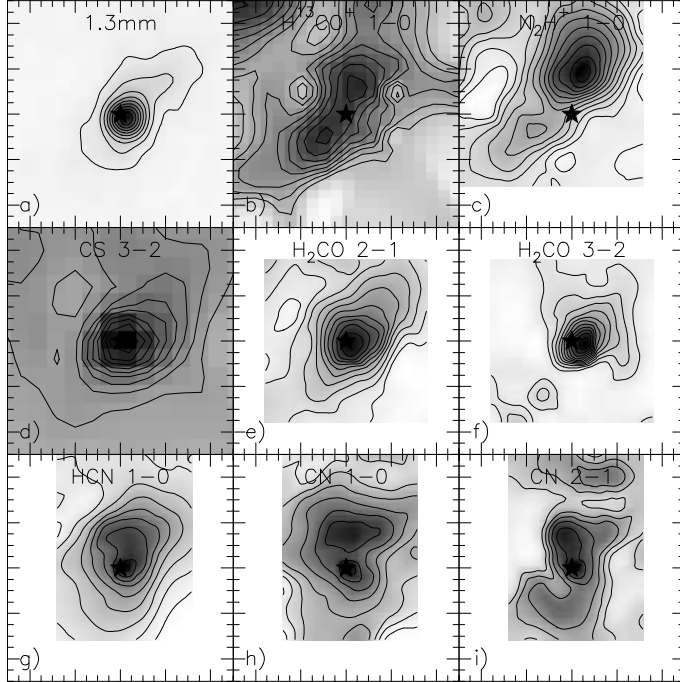


Fig. 5. Same as Fig. 1 for LkH α 234. Contour levels are: a) 39.2 mJy/beam, 78.5 to 706.2 mJy/beam by steps of 78.5 mJy /beam ; b) 0.19 to 1.7 by 0.19 K kms $^{-1}$; c) 0.2 to 8.2 by 0.4 K kms $^{-1}$; d) 1.5 to 15 by 1.5 K kms $^{-1}$; e) 1 to 11 by 1 K kms $^{-1}$; f) 1.5 to 16.5 by 1.5 K kms $^{-1}$; g) 2 to 11 by 1 K kms $^{-1}$; h) 0.5 to 5 by 0.5 K kms $^{-1}$; i) 1 to 6 by 1 K kms $^{-1}$

the high velocity components. The derived densities and column densities are shown in Table 6. We are aware that the NH $_3$ and SiO emissions could arise in different regions and the assumed kinetic temperatures are very uncertain. But since the SiO lines are optically thin, the derived column densities are weakly dependent on the assumed kinetic temperature and are accurate within a factor of ~ 2 . The values of Table 6 clearly show that the SiO abundance is larger by almost 2 orders of magnitude in the high velocity gas of FIRS 2-out 1 than in the narrow component associated with FIRS 2-out 2. Within FIRS 2-out 1, we also detect a gradient in the SiO abundance, being the SiO/ ^{13}CO ratio 2 orders of magnitude larger in the high velocity component than in the ambient component. This enhancement of the SiO abundance in the high velocity gas is also observed in very young low-mass protostellar outflows (Bachiller et al. 1991, 2001) and interpreted as due to the chemical gas processing by the energetic shocks associated with the high velocity “bullets”.

Hydrogen densities are also quite independent on the assumed temperature for $T_k > 50$ K. The estimated hydrogen density decreases by only a factor of ~ 4 if we change the kinetic temperature from 15 K to 100 K. Thus, the estimated hydrogen densities are accurate within a factor of ~ 4 . Our calculations show that the density seems to increase from a few 10^5 cm $^{-3}$ in the ambient component to

$> 10^6$ cm $^{-3}$ in the high velocity gas at the star position. We have also carried out LVG calculations for R1 and B1, and at the offset (50'', -50'') where only the narrow component has been detected. The density in the bullets R1 and B1 is $\gtrsim 10^5$ cm $^{-3}$ while the density in the narrow component detected at the offset (50'', -50'') is of a few 10^4 cm $^{-3}$. This density is an upper limit to the hydrogen density in the narrow component, since the kinetic temperature is never expected to be lower than 15 K. Thus, we consider that the estimated difference in the hydrogen density of the wide and narrow components is reliable. The lower density of the narrow component also supports our interpretation of the SiO emission arising in the gas of the molecular cloud surrounding the outflow.

We have observed a map of $80'' \times 80''$ around LkH α 234 in the SiO 2 \rightarrow 1 and 3 \rightarrow 2 lines. We have detected SiO emission only towards the star position. Since we have integrated double time towards the star position than in the other map positions, we cannot exclude the possibility of SiO emission at the same level in other positions. Thus we have poor information about the spatial distribution of the emission. Regarding the kinematical information, the large linewidth of the SiO lines, $\Delta v > 3$ km s $^{-1}$, compared to that of the (1,1) and (2,2) ammonia lines suggests that the emission arises in the warm component. The weakness of the SiO 2 \rightarrow 1 line emission as well as the

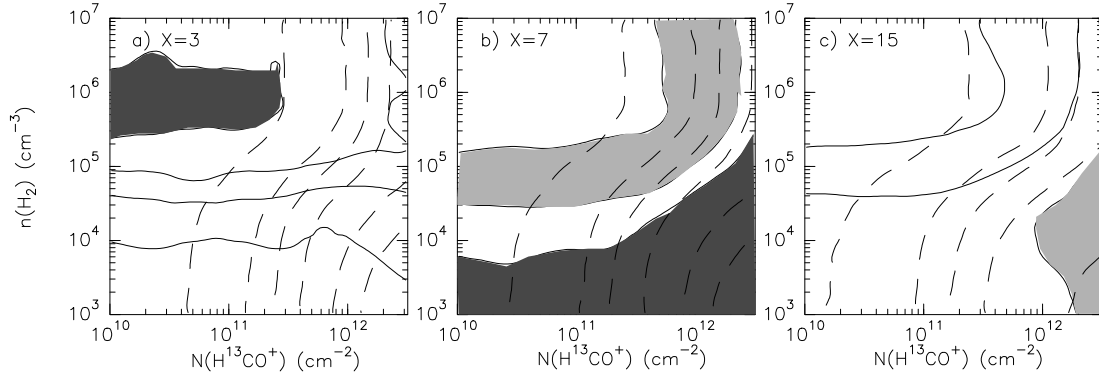


Fig. 6. Plots of the $r_1 = I(N_2H^+)/I(H^{13}CO^+)$ ratio and opacity of the main N_2H^+ hyperfine component (solid contours), and τ_m (dashed contours), as a function of the $H^{13}CO^+$ column density, $N(H^{13}CO^+)$, and hydrogen density, n , for a kinetic temperature of $T_k = 15K$ and an $N_2H^+/H^{13}CO^+$ abundance ratio, $X=3,7,15$. We have shaded with dark grey the region with $r_1 = 1.5 \pm 0.3$ (ratio measured at the $32''$ offset from the star position) and with a clear color $r_1 = 2.7 \pm 0.6$ (ratio measured at the star position). We need a depletion of at least a factor of 2 towards the center in order to fit both τ_m and r_1 in both positions. Contour levels are: a) $r_1 = 0.8, 1, 1.2$ and $\tau_m = 0.1, 0.5, 1.0, 2, 5, 10$; b) $r_1 = 1.8, 2.2, 2.7, 3.2$ and $\tau_m = 0.1, 0.5, 1.0, 2, 5, 10$; c) $r_1 = 3.2, 5, 7$ and $\tau_m = 0.1, 0.5, 1.0, 2, 5, 10$

lack of information about the source size make any estimate of the hydrogen density very uncertain. We have derived the SiO column density assuming $n \sim 5 \cdot 10^5 \text{ cm}^{-3}$. With this assumption we derive a SiO column density of $\sim 10^{11} \text{ cm}^{-2}$. This value is lower by a factor of >6 than the total SiO column density towards FIRS 2. The SiO/ ^{13}CO ratio towards this star is similar to that found in PDRs (Schilke et al. 2001).

In Table 7 we present a summary of the SiO observations. There is a clear evolutionary trend in the SiO behavior. The youngest outflow FIRS 2-out 1 presents intense SiO emission at high velocity with SiO abundances as high as $\sim 10^{-8}$. Towards the more evolved outflow FIRS 2-out 2 we have detected only a weak SiO line at ambient velocity. The SiO abundance in this component is $\sim 10^{-10}$, i.e., two orders of magnitude lower than the SiO abundance in the high velocity gas associated with FIRS 2-out 1 but still larger than the SiO abundance in PDRs and dark clouds. Towards LkH α 234 we have detected SiO emission at the ambient velocities with a fractional abundance of 10^{-12} . This abundance is similar to that measured in PDRs and could be associated with the PDR produced by LkH α 234.

This evolutionary trend confirms that SiO is a good tracer of energetic shocks. The SiO abundance is highly enhanced when the shocks are strong enough to release the silicon from the grains to the gas phase (Martín-Pintado et al. 1992). In a MHD shock model the release of Si to the gas phase requires $V_{shock} > 40 \text{ km s}^{-1}$ (Flower, Pineau des Forets, Field, & May 1996). This is consistent with the trend of having larger SiO abundances in the higher velocity gas. Because of projection effects, the velocity we measure is a lower limit to V_{shock} . As the protostar evolves, the outflow fades and the amount of high velocity molecular gas decreases. This produces a

Table 7. SiO emission

| Outflow | Age (Myr) | Component | $X(\text{SiO})^3$ |
|------------------|--------------------|---------------|----------------------------|
| FIRS 2-out 1 | 0.003 ¹ | High velocity | $\sim 10^{-8}$ |
| FIRS 2-out 2 | 0.005 ¹ | Ambient | $\sim 10^{-10}$ |
| LkH α 234 | $\sim 0.1^2$ | Ambient | $\sim 10^{-12} - 10^{-11}$ |

¹ Estimated age of the outflow assuming a velocity of 15 km s^{-1} and the lobe sizes measured from Fig. 1.

² Stellar age from Fuente et al. (1998)

³ Fractional abundance estimates assuming $X(^{13}CO) = 2 \cdot 10^{-6}$ and $X(H^{13}CO^+) = 10^{-10}$

decrease in the SiO abundance. When the bipolar molecular outflow stops, the SiO abundance around the star decreases to the typical value in PDRs.

5.4. CS, C³⁴S

We have carried out a map of the CS 3 \rightarrow 2 emission towards FIRS 2 and LkH α 234. In addition we have observed the C³⁴S 2 \rightarrow 1, 3 \rightarrow 2 and 5 \rightarrow 4 lines towards the (0,0) position. The spectra towards the (0,0) position are shown in Fig. 9 and the Gaussian fits are shown in Tables 2 and 3. The integrated intensity maps of the CS J=3 \rightarrow 2 line are shown in Fig. 4.

Similarly to the case of SiO, the profiles of the CS and C³⁴S lines towards FIRS 2 present high velocity wings at red-shifted velocities. However, the terminal velocity of these wings is lower than those of the SiO lines. The velocity range of the CS emission is between -14 and -5 km s^{-1} , i.e., it is only detected at the ambient velocities and in the moderate velocity component of the SiO emission. The spatial distribution of this component in the CS

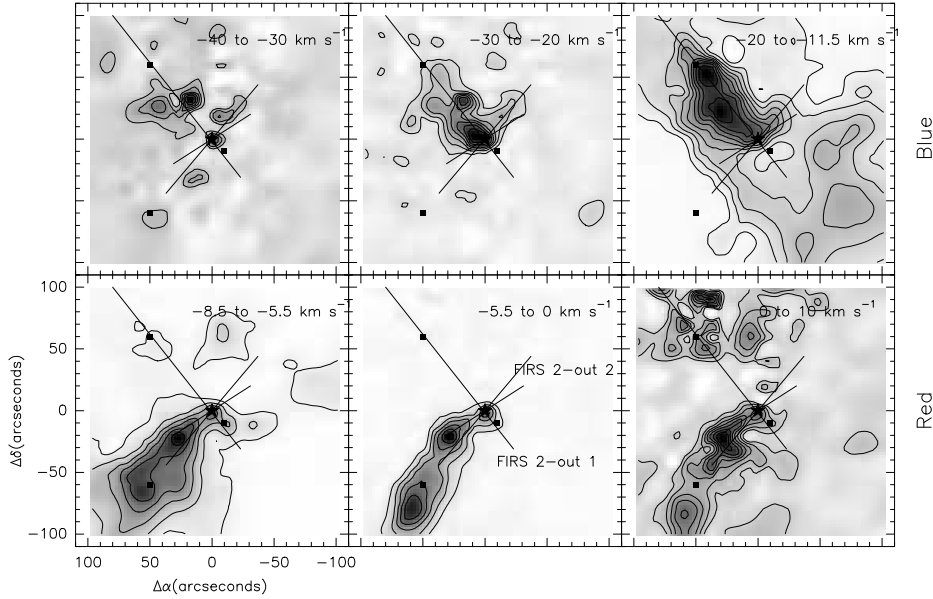


Fig. 7. High velocity CO emission in FIRS 2. The blue-shifted velocities are shown in the top panels, and the red-shifted velocities in the bottom panels. Straight lines indicate the outflow axis. In the case of FIRS 2-out 2 we have drawn two axis because of outflow precession. Contour levels are: a) 1 to 6 by 1 K kms⁻¹; b) 2 to 22 by 2 K kms⁻¹; c) lev 7 to 70 by 7 K kms⁻¹; d) 7 to 80 by 7 K kms⁻¹; e) 4 to 50 by 4 K kms⁻¹; f) 1 to 8 by 1 K kms⁻¹.

3→2 line is different from that of the same component of the SiO emission, suggesting that both molecules might be tracing different gas components even when comparing the same velocity range.

We have carried out LVG calculations to estimate the physical conditions of the gas emitting in CS. Different line ratios are found at the ambient velocities and in the moderate velocity range in the C³⁴S lines (see Fig. 9). Thus, we have estimated the physical conditions in the two velocity intervals. We have derived a density $\geq 3 \cdot 10^6 \text{ cm}^{-3}$ for the ambient component in FIRS 2. This density is larger by a factor ~ 6 than the density estimated from SiO lines. This difference is not due to the assumed kinetic temperature, since even assuming a kinetic temperature of 100 K the density would decrease only by a factor of ~ 4 . However, the densities derived from the C³⁴S lines in the moderate range are similar to those derived from the SiO lines. We propose that at least part of the C³⁴S lines emission at ambient velocities does not arise in the outflow. We speculate with the possibility of the C³⁴S emission arising in a hot core.

The CS and C³⁴S lines observed in LkH α 234 are shown in Fig. 9. The line-widths of the C³⁴S lines are similar to that of the SiO and the NH₃ (3,3) lines suggesting that they are tracing a warm component. The emission of the CS lines is concentrated towards the star position, therefore the connection between the outflow and the CS emission is not clear. We have derived a density $\sim 10^5 \text{ cm}^{-3}$ for this warm component. This density is lower than the typical density of the hot cores associated with

massive stars. Since LkH α 234 is a visible star, the envelope has already been disrupted by the star and the UV radiation is escaping through the envelope. A dense ($n > 10^6 \text{ cm}^{-3}$) hot region similar to the hot cores in massive stars is not expected at this evolutionary stage.

5.5. CH₃OH

We have observed up to 17 methanol lines towards the (0,0) position in FIRS 2 and LkH α 234. The large number of lines allows us to have a good estimate of the rotation temperature and the CH₃OH column density. In addition, we have obtained a small map in the intense CH₃OH 2→1 and 5→4 lines towards FIRS 2. The CH₃OH maps around FIRS 2 are shown in Fig. 4. The CH₃OH emission peaks towards the bullet R1 suggesting that these lines arise mainly in the molecular outflow.

The high-velocity resolution spectra of the CH₃OH lines are shown in Fig. 10. The velocity profiles of the CH₃OH lines towards FIRS 2 are similar to those found in the SiO lines. The low energy lines present two velocity components, a narrow component at the ambient velocity and a wide wing which extends to red-shifted velocities and is centered at $-6 \pm 1 \text{ km s}^{-1}$. In higher energy transitions, the narrow component becomes weaker and only the wide red-shifted one is detected. This is consistent with the integrated intensity maps of the CH₃OH 2→1 and 5→4 lines shown in Fig. 4 which show a strong peak emission at the position of the bullet R1. In order to further investigate the nature of the CH₃OH emission, we

Table 6. LVG calculations : SiO

| Source | Vel. range (km s ⁻¹) | T _k (K) (K) | n (cm ⁻³) | N(¹³ CO) (cm ⁻²) | N(SiO) (cm ⁻²) | N(H ¹³ CO ⁺) (cm ⁻²) | SiO/ ¹³ CO | SiO/H ¹³ CO ⁺ |
|------------------------------------|-------------------------------------|---------------------------|--------------------------|---|-------------------------------|--|-----------------------|-------------------------------------|
| FIRS 2 (Star) | -13.5 – -11.5 | 50 | 5 10 ⁵ | | 1.5 10 ¹¹ | 1.0 10 ¹¹ | | 1.5 |
| | -11.5 – -8.5 | 15 | 5 10 ⁵ | | 1.1 10 ¹² | 1.5 10 ¹² | | 0.7 |
| | -8.5 – -4.5 | 50 | 4 10 ⁵ | | 1.2 10 ¹² | | | |
| | -4.5 – -0.5 | 50 | 1 10 ⁶ | | 4.7 10 ¹¹ | | | |
| | Total | | | | 2.8 10 ¹² | 1.5 10 ¹² | | 1.9 |
| (-10'',-10'') R1 (FIRS 2-out 1) | -13.5 – -11.5 | 50 | 5 10 ^{5*} | 3 10 ¹⁵ | 4 10 ¹¹ | | 0.0001 | |
| | -11.5 – -8.5 | 15 | 4 10 ⁵ | 4 10 ¹⁶ | 3 10 ¹² | 1 10 ¹² | 0.00007 | 3 |
| | -8.5 – -4.5 | 50 | 4 10 ⁵ | 3 10 ¹⁵ | 1.5 10 ¹² | | 0.0005 | |
| | -4.5 – -0.5 | 50 | 3 10 ⁴ | 3 10 ¹⁴ | 1.5 10 ¹² | | 0.005 | |
| | Total | | | 4.6 10 ¹⁶ | 6.4 10 ¹² | 1 10 ¹² | 0.0001 | 6 |
| (50'',50'') B1 (FIRS 2-out 1) | -17.5 – -12.5 | 50 | 2 10 ⁵ | 1.5 10 ¹⁵ | 1.5 10 ¹² | | 0.001 | |
| | -12.5 – -8.5 | 50 | 2 10 ⁵ | 5.5 10 ¹⁶ | 1.5 10 ¹² | | 0.00003 | |
| | -8.5 – -4.5 | 50 | 2 10 ⁵ | 2.0 10 ¹⁵ | 2.0 10 ¹¹ | | 0.0001 | |
| | Total | | | 5.8 10 ¹⁶ | 3.2 10 ¹² | < 2 10 ¹² | 0.00005 | > 1 |
| (50,-50) O2 (FIRS 2-out 2) | -11.5 – -8.5 | 15 | 8 10 ⁴ | | 1.0 10 ¹¹ | 3 10 ¹¹ | | 3 |
| LkHα 234 (IRS 6-out 1) | -12.5 – -8.5 | 50 | 5 10 ^{5*} | 1.3 10 ¹⁷ | 2.0 10 ¹¹ | 1.0 10 ¹² | 0.000001 | 0.2 |

* Assumed value for the hydrogen density

Table 8. LVG calculations : CS, C³⁴S

| Source | Vel. range | T _k (K) | n (cm ⁻³) | N ^s (C ³⁴ S)(cm ⁻²) | Ω _s |
|-------------------|---------------------------------|--------------------|-----------------------|---|----------------|
| NGC 7129 – FIRS 2 | -10.5 – -9.5 km s ⁻¹ | 15 | 3 10 ⁶ | 8.0 10 ¹¹ | ~9'' |
| | -9.5 – -6.5 km s ⁻¹ | 50 | 6 10 ⁵ | 7.1 10 ¹¹ | ~4'' |
| | Total | | | 1.5 10 ¹² | |
| LkHα 234 | -11.5 – -9.5 km s ⁻¹ | 50 | 2 10 ⁵ | 9.6 10 ¹¹ | 14'' |
| | -9.5 – -5.5 km s ⁻¹ | 50 | 4 10 ⁵ | 7.8 10 ¹¹ | 6'' |
| | Total | | | 1.7 10 ¹² | |

have fit the lines with Gaussian profiles and make some correlations. In Fig. 11 we plot the central velocity and linewidths of the CH₃OH lines vs. the upper state energy of the observed transition. It is clearly seen that the linewidths of the CH₃OH lines increase with the upper state energy of the transition at moderate energies. In fact, they increase from ~3 km s⁻¹ in the low energy transitions to ~7 km s⁻¹ in transitions with E_u>50 K. But this trend is not valid for higher energy lines which seem to have a constant linewidth of ~4 km s⁻¹. A similar behavior is found when one compares the velocity of the line with the upper state energy. The line velocity changes from v~-10 km s⁻¹ to ~-7.5 km s⁻¹ when the energy increases from ~10 K to 50 K. However, for higher energies, the line velocities seem to make the reverse way and change from ~-8 km s⁻¹ to -10 km s⁻¹. This suggests that the emission of the low and moderate energy transitions (E_u>50 K) arise in the molecular outflow. The correlation found between the linewidth and the energy of the transition suggests that the high velocity gas is asso-

ciated with higher excitation temperatures. This result is consistent with the density estimated from the SiO lines. For E_u> 50 K, there is a jump in the line velocity which go back to ~ -10 km s⁻¹. We propose that this could be due to the existence of a hot component in the CH₃OH emission in addition to that related to the bipolar outflow.

In Fig. 11 we show the CH₃OH rotational diagram for FIRS 2. All the observed CH₃OH transitions cannot be fitted with a single straight line. We need to assume at least two rotation temperatures to fit the observational data. The low energy transitions (E_u<50 K) are well fit with a T_{rot}~17 K, while the high energy transitions require a higher rotation temperature, T_{rot}>80 K. We propose the existence of a “hot core” component which dominates the emission in the high energy transitions.

Several CH₃OH lines have also been observed in LkHα 234. In this case all the lines are centered at the ambient velocity. However, there are important variations in the linewidths of the observed lines. Like in the case of FIRS 2, the linewidths seem to increase with the energy

of the upper level for $E_u < 50$ K (see Fig. 12). We have only detected the methanol lines towards the (0,0) position and consequently, we have no information about the size of the emitting region. Thus, we have considered the two limiting cases of a point source and a beam filling factor of 1 to make the rotational diagram. In the first case, we need two gas components to fit all the observed transitions. The cold one would have $T_{rot} \sim 24$ K, and the hot one, $T_{rot} > 250$ K. But if we assume a beam filling factor of 1, all the observed transitions are well fit with a $T_{rot} \sim 60$ K. With our data, we cannot discern between these two cases.

5.6. H_2CO

We have observed two H_2CO rotational transitions and one of the rarer isotope $H_2^{13}CO^+$ toward FIRS 2 and LkH α 234. The obtained spectra are shown in Fig. 10. Similarly to other molecules, the H_2CO spectra towards FIRS 2 present two well differentiated components, a narrow one centered at ~ -9.6 km s $^{-1}$ with a linewidth of ~ 1.3 km s $^{-1}$ and a much wider one centered at ~ -9.0 km s $^{-1}$. However, the wide component has not the typical R1 profile observed in the SiO, CS and methanol lines at the star position. While the profiles of the SiO, CS and methanol lines present only red wings, the H_2CO lines present a quite symmetric profile with blue and red wings. Consequently, the central velocity of the wide H_2CO component is similar to that of the ambient gas and the linewidth is as large as $\Delta v = 7$ km s $^{-1}$. To further investigate the nature of these components we have studied the integrated intensity maps of the H_2CO $2_{12} \rightarrow 1_{11}$ line for the different velocity intervals (see Fig. 13). The most striking feature could be the jet-like morphology observed in the H_2CO emission at blue velocities (from -15 to -10 km s $^{-1}$). At red velocities, the emission is maximum at the offset (-7'', -7'') which is located close to the bullet R1. Since the wide component have a very well differentiated profile, we have been able to subtract the wide component to the observed spectra and mapped both components separately. Our results are quite suggestive. The wide component presents a jet-like morphology with the maximum towards the position R1. The morphology of the narrow component is an intense ridge which surrounds the jet. This strongly suggests that the narrow component is tracing the shocked gas of the molecular cloud which is interacting with the jet. The maximum of this narrow component coincides with the position where the bullet R1 impinges in the cloud. We have derived rotation temperatures and column densities in the narrow and wide components separately, and obtained similar excitation conditions in both components. Thus, although the kinematics is clearly different, the physical condition of both components are quite similar.

In Fig. 10 we show the H_2CO spectra towards LkH α 234. The profiles of the H_2CO lines in this source, also suggest the existence of a narrow and wide components.

However, these two component cannot be easily separated. For this reason, we have derived rotation temperatures by considering the sum of the two components. We obtain a rotation temperature and H_2CO column density similar to those obtained in FIRS 2. In Fig. 5 we show the integrated line intensity maps in this source. Similarly to the case of FIRS 2 we find emission along the outflow and in a direction perpendicular to it. Thus far, no bipolar outflow has been detected in this direction. Thus, this H_2CO emission is associated with the flattened clump in which the Herbig Be star LkH α 234 is embedded that is being heated by the recently born star.

5.7. CH_3CN

We have observed the CH_3CN $5 \rightarrow 4$ and $13 \rightarrow 12$ lines towards FIRS 2 and LkH α 234. Because of the rotational structure of CH_3CN , one can observe several lines at different energies very close in frequency. This allows us to estimate the rotation temperature avoiding observational errors and the uncertainty due to the unknown source size. We have carried out these calculations towards our two sources. Unlike the other molecules observed, we do not detect a cold component in the CH_3CN lines, but only the warm one. The detection of a hot CH_3CN component with $T_k > 63$ K in FIRS 2 shows the existence of a hot core in this object.

CH_3CN seems to be the best tracer of hot cores in these intermediate-mass stars. Contrary to CH_3OH and H_2CO whose low energy lines arise mainly in the bipolar outflow, the rotational lines of CH_3CN seems to arise in the hot core and provide a good measure of the kinetic temperature of this hot component.

5.8. CN, HCN

We have mapped a small region around FIRS 2 and LkH α 234 in the HCN $1 \rightarrow 0$ and CN $1 \rightarrow 0$ and $2 \rightarrow 1$ lines. The integrated intensity maps around FIRS 2 are shown in Fig. 4 and 5. Thus far, we have two different kind of molecules depending on the morphology of their emission in FIRS 2. The first group is formed by the molecular ions N_2H^+ and $H^{13}CO^+$ which peak at the YSO position and trace the bulk of the cold envelope. The second group is formed by CS, SiO, CH_3OH and H_2CO peaks at the position R1 and its emission has an important contribution from the molecular outflow FIRS 2-out 1. The morphology of the CN $1 \rightarrow 0$ emission is different from those of these two groups. The CN emission does not peak at the star position nor at the position of the bullet R1, but to the north, suggesting a new chemical differentiation in the protostellar envelope. The morphology of the HCN emission is also different from those of the other molecular lines. In fact, the HCN emission peaks to the NW from the star position, in a position intermediate between the bullet R1 and the peak of the CN emission. The large linewidths of the HCN $1 \rightarrow 0$ line (see Fig. 15) show that, in contrast to the CN $1 \rightarrow 0$ line,

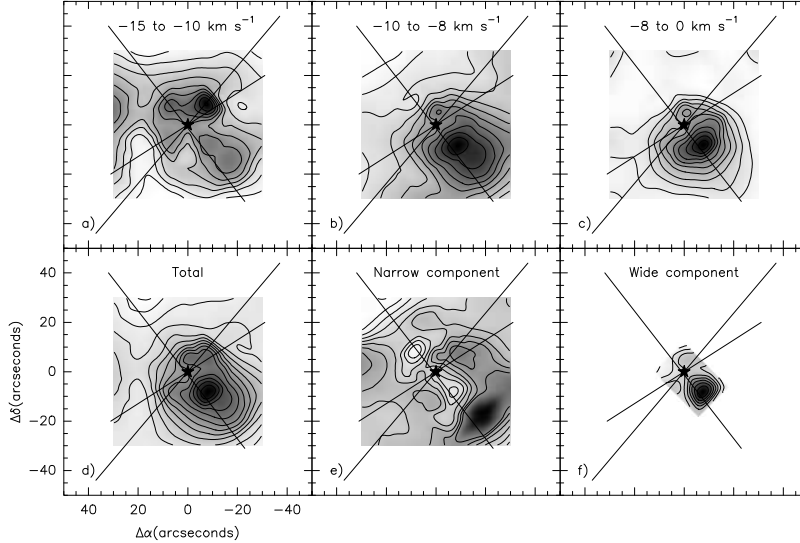


Fig. 13. Panels a-d are the integrated intensity maps of the $\text{H}_2\text{CO } 2_{12}\rightarrow 1_{11}$ line towards NGC 7129 – FIRS 2 for different velocity intervals. In panel e) we show the integrated intensity map of the H_2CO lines after subtracting the Gaussian fit to the wide component from all the spectra. In panel f) we show the area of this wide component as derived from the Gaussian fit. The axis of the outflow FIRS 2-out 1 and FIRS 2-out 2 are indicated. Contour levels are: a) 0.5 to 5 by 0.5 K km s^{-1} ; b) 1.0 to 6.5 by 0.5 K km s^{-1} ; c) 0.5 to 5 by 0.5 K km s^{-1} ; d) 1 to 14 by 1 K km s^{-1} ; e) 0.5 to 5 by 0.5 K km s^{-1} ; f) 1 to 11.5 by 1 K km s^{-1} .

the emission of the $\text{HCN } 1\rightarrow 0$ line has a significant contribution from the molecular outflow giving rise to this peculiar morphology.

The radicals CN and HCN are known to be specially abundant in PDRs. In particular, the CN/HCN ratio has been successfully used as a PDR tracer in different kind of objects. In Fig. 16, we show the maps of the $(\text{CN } 1\rightarrow 0)/(\text{HCN } 1\rightarrow 0)$ intensity ratio in FIRS 2 and LkH α 234. The $(\text{CN } 1\rightarrow 0)/(\text{HCN } 1\rightarrow 0)$ line intensity ratio is maximum at the star position and to the north, forming a conical feature with the star at its apex. We have been estimated the CN rotation temperature from the $(\text{CN } 2\rightarrow 1)/(\text{CN } 1\rightarrow 0)$ line intensity ratio (see Table 4). Assuming the LTE approximation and the same rotation temperature for CN and HCN, we obtain a CN/HCN abundance ratio of ~ 3 at the star position. This value is similar to those found in PDRs and suggests that the gas chemistry in this conical feature is being affected by the UV radiation from the protostar. However, the axis of this conical feature seems to be more similar to that of the outflow FIRS 2-out 2 than to that of the outflow FIRS 2-out 1. This suggests that the PDR traced by the high CN/HCN ratio could be related to the star driving the outflow FIRS 2-out 2 instead of to the Class 0 object. In fact, the PDR could be formed in the walls of the cavity excavated by the outflow FIRS 2-out 2 when they are illuminated by the exciting star. But observations with higher spatial resolution are required to conclude about this point.

We have also observed the CN and HCN lines towards LkH α 234. In this case, the linewidths of the CN and HCN

lines are similar, and in agreement with those found in the warm component. But, contrary to most of the observed molecular species, the CN and HCN emission do not peak at the star position but to the north forming a conical feature. We have calculated the CN/HCN integrated intensity ratio in the region. Surprisingly, the CN/HCN ratio is minimum at the star position and maximum at the border of the clump as traced by the 1.3mm observations suggesting that the clump is illuminated from outside. Making column densities estimates, we derive $N(\text{CN})/N(\text{HCN})\sim 3$ at the star position.

Thus, the CN/HCN fractional abundance ratio at the star position is equal (within the uncertainties) in FIRS 2 and LkH α 234 and consistent with the expected value in a PDR. However the behavior of the CN/HCN ratio is very different in the rest of the envelope. In the case of FIRS 2, the CN/HCN ratio decreases outwards from the star as expected from a PDR illuminated from the interior and with an optically thick envelope. In the case of LkH α 234, the CN/HCN ratio is quite constant inside the clump and increases at the edges. This suggests that the clumps is also illuminated from outside (the clump is located at the border of an HII region). Since the envelope is less massive than that associated with FIRS 2, the whole envelope can be considered as a PDR.

6. Deuterated compounds

In order to derive the deuterium fractionation we have observed the $\text{DCO}^+ 2\rightarrow 1$ and $3\rightarrow 2$, $\text{N}_2\text{D}^+ 3\rightarrow 2$, and $\text{D}_2\text{CO } 4_{04}\rightarrow 3_{03}$ lines toward the studied regions. In Fig. 15

we show the spectra of these lines toward FIRS 2 and LkH α 234. The integrated line intensity maps of the DCO $^+$ 2 \rightarrow 1 line toward FIRS 2 are shown in Fig. 4.

The linewidths of the DCO $^+$ and N $_2$ D $^+$ lines are ~ 1.0 km s $^{-1}$ suggesting that they arise in the cold component of the envelope like the non-deuterated compounds HCO $^+$ and N $_2$ H $^+$. The linewidth of the D $_2$ CO line is ~ 4 km s $^{-1}$ like those of the lines arising in the warm component, and in particular, the lines of the chemically related species H $_2$ CO and H $_2$ 13 CO. In Table 9 we show the DCO $^+$ /H 13 CO $^+$, N $_2$ D $^+$ /NH $_2^+$ and D $_2$ CO/H $_2$ CO abundance ratios in both sources. The DCO $^+$ /H 13 CO $^+$ abundance ratio is a factor of 20 lower in LkH α 234 than in FIRS 2. This factor is so large that cannot be due to the H 13 CO $^+$ depletion but to a different value of the deuterium fractionation in these cold envelopes. Thus, we propose that the deuterium fractionation in the cold envelope decrease during the protostellar evolution. As we will comment in detail in next section, this increase in the deuterium fractionation can be understood as the consequence of the envelope warming during the protostellar evolution.

A very different case is the D $_2$ CO/H $_2$ CO abundance ratio which increases by a factor ~ 1.5 from FIRS 2 to LkH α 234. Since a factor of 1.5 is within the uncertainties of our column density estimates, we conclude that the deuterium fractionation, as measured by the D $_2$ CO/H $_2$ CO abundance ration, seems to be constant (or slightly increase) in the warm component during the protostellar evolution. Thus, the evolution of the deuterium fractionation in the warm envelope seems to follow a different trend than in the cold envelope. The evaporation of the icy grain mantles is very likely the main responsible of this behavior.

7. Discussion

7.1. Physical structure of the YSOs envelopes and its evolution

Our data show the existence of at least two well differentiated components in the envelope of FIRS 2 and LkH α 234, the cold envelope traced by the low energy lines of NH $_3$, N $_2$ H $^+$ and H 13 CO $^+$, and the warm envelope traced by the CS, CH $_3$ OH and H $_2$ CO lines. These two components can be differentiated observationally by their kinematics, the morphology of their emission and by their physical conditions. Thus the lines arising in the cold component are narrow ($\Delta v \sim 1$ km s $^{-1}$) and the emission peak is located at the star position in FIRS 2. Besides, the kinetic temperature of this gas estimated from the NH $_3$ lines is ~ 13 K in FIRS 2 and ~ 28 K in LkH α 234.

A warm envelope component is detected towards these sources traced by the emission of species like CS, CH $_3$ OH and H $_2$ CO. These species present enhanced abundances in regions where the icy grain mantles are evaporated (van der Tak et al. 2000). They are also abundant in molecular outflows where they can be released to the gas

phase by shock fronts. In FIRS 2, the emission of the low energy transitions of these species arise mainly in the bipolar outflow. However, this association is not clear in LkH α 234 where their emission could arise in the inner and warmer part of the envelope.

Finally, we have strong evidences for the existence of a hot core in the Class 0 protostar FIRS 2. The high density measured at ambient velocities from the C 34 S lines, the high temperature component of the CH $_3$ OH lines and, above all, the detection of the CH $_3$ CN lines with rotation temperature of ~ 63 K show the existence of a hot core in this target.

7.2. Physical and Chemical evolution of the YSOs envelopes

7.2.1. Cold envelope

In Table 9, we show the physical parameters and molecular column densities in the Class 0 protostar FIRS 2 and LkH α 234. The molecules NH $_3$, N $_2$ H $^+$, H 13 CO $^+$ and their deuterated compounds DCO $^+$ and N $_2$ D $^+$ trace the cold envelope component. The column densities of these species decrease by a factor of 5–10 from the Class 0 protostar to the Type I Herbig Be star showing that the mass of the cold envelope decrease by at least a factor of 5 during the protostellar phase. Based on the NH $_3$ and N $_2$ H $^+$ data we have also derived the kinetic temperature and size of this cold component. The kinetic temperature increases from ~ 13 to ~ 28 K and the size of the emitting region decreases from 21'' to 6'' from FIRS 2 and LkH α 234. This is consistent with previous results by Fuente et al. (2002) which shows the protostellar envelope is dispersed and becomes warmer during its evolution to become a visible star.

The warming of the cold envelope produces changes in its chemical composition. In Table 5 we show the N $_2$ H $^+$ /H 13 CO $^+$ and NH $_3$ /N $_2$ H $^+$ abundance ratios in several positions. Note that the N $_2$ H $^+$ /H 13 CO $^+$ ratio is different in the studied objects. The N $_2$ H $^+$ /H 13 CO $^+$ ratio is ~ 17 in the cold young object FIRS 2 and ~ 6 in the more evolved and warmer Herbig Be star LkH α 234. As discussed in Section 3.2, this gradient in the N $_2$ H $^+$ /H 13 CO $^+$ ratio is very likely due to the H 13 CO $^+$ depletion in the cold envelope of the protostar. Molecular depletion is expected to be significant only for kinetic temperatures $T_k < 20$ K. Thus, molecular depletion is negligible in the envelope of LkH α 234 where the gas kinetic temperature is ~ 28 K.

Within the nitrogen chemistry, we have also studied the NH $_3$ /N $_2$ H $^+$ ratio. Since the beam is very different for the NH $_3$ and N $_2$ H $^+$ observations, this abundance ratio is very dependent on the assumed source size. For LkH α 234 we have been able to calculate both, the NH $_3$ and N $_2$ H $^+$ emitting regions sizes. We have derived the same size, $\sim 6''$ – $8''$, for both molecules and the NH $_3$ /N $_2$ H $^+$ ratio is ~ 10 . In the case of FIRS 2 we have not been able to derive the source size from the NH $_3$ emission but we have estimated a size of $\sim 21''$ from the N $_2$ H $^+$ observations. We have assumed two limiting cases for the calcu-

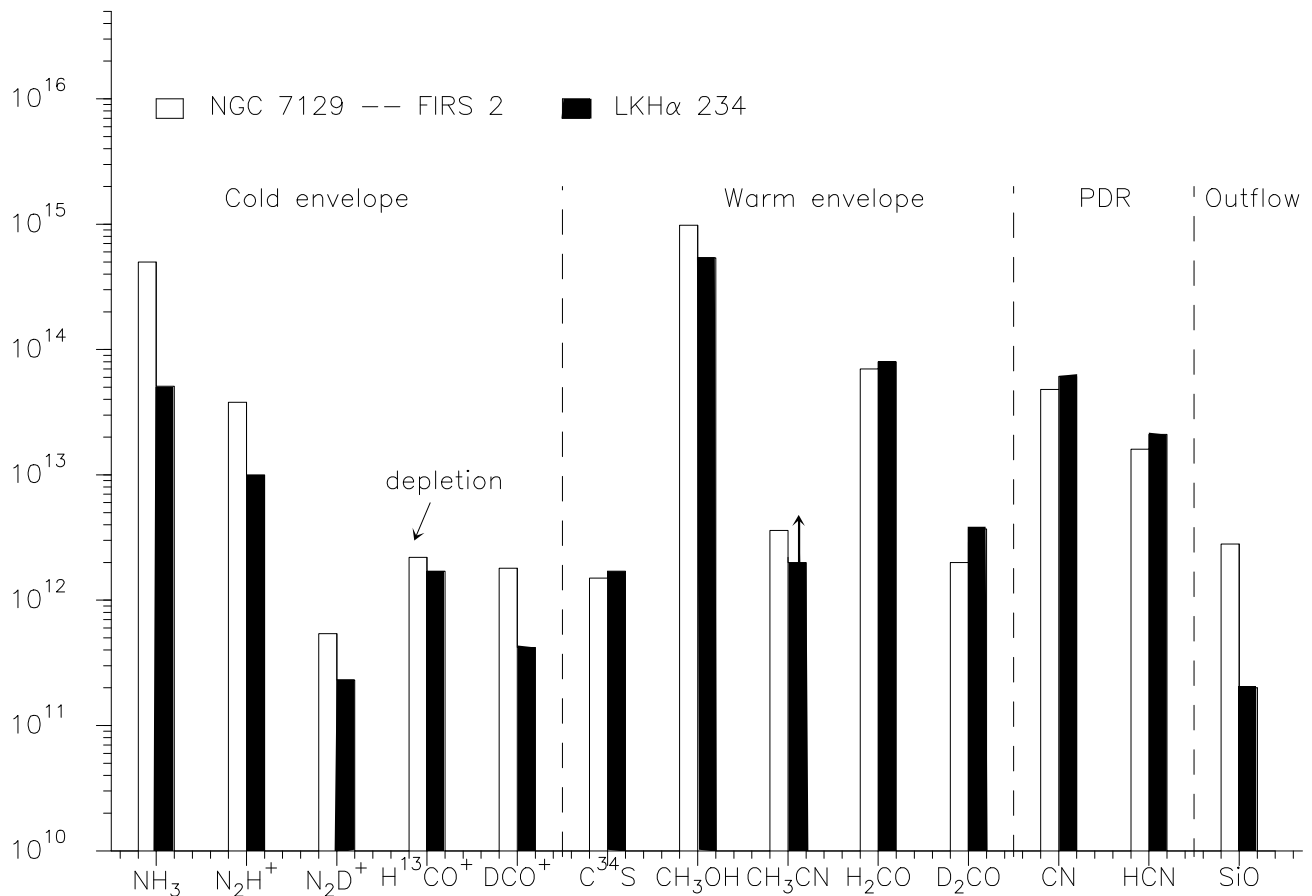


Fig. 17. Histogram with the total beam-averaged molecular column densities estimated in the IM Class 0 YSO NGC 7129 – FIRS 2 and the HBe star LkH α 234. The column densities of the molecules tracing the cold envelope decrease at least by a factor of 5 between NGC 7129–FIRS 2 and LkH α 234. An exception is H¹³CO⁺ that is depleted in the Class 0 protostar (see text). The column densities of the molecules tracing the warm envelope and the PDR remain quite constant, in some cases increase, from the Class 0 protostar to the HBe star. The SiO column density is lower by almost 2 orders of magnitude in LkH α 234 than in NGC 7129–FIRS 2. This is very likely related to the absence of an energetic bipolar outflow in the HBe star.

lations of the NH₃/N₂H⁺ ratio in this source. Assuming a beam filling factor of ~ 1 for both molecules we obtain NH₃/N₂H⁺ ~ 13 in this object. However if we assume that the size of the NH₃ emission is $\sim 21''$, like in the case of N₂H⁺, we obtain NH₃/N₂H⁺ ~ 33 . In this case, we would have an NH₃ abundance enhancement in the colder envelope of the Class 0 protostar. Recent results in pre-stellar core show that the NH₃ abundance could be enhanced in dense regions of these cores where the CO is expected to be depleted (Tafalla et al. 2004).

7.2.2. Warm envelope

When the star heats the envelope a sublimation front proceeds outwards the star removing molecules from grain mantles. The region of the envelope in which the gas kinetic temperature is high enough to evaporate the grain mantles is what we have called “warm envelope”. The

species released to gas phase are called “parent molecules” and increase significantly their abundances. The molecules CH₃OH, NH₃, and H₂CO are within this group. These molecules drive a high temperature chemistry giving rise to “daughter” molecules like CH₃CN. Within this scheme, CH₃OH, H₂CO and CH₃CN are tracers of the warm part of the envelope where the ices have been evaporated (Rodgers & Charnley 2003). Some of these species are also abundant in the molecular outflow where shock fronts remove them from the grains mantles, and to a lesser extent in the cold envelope. This is the case for NH₃ with the emission of the low-lying transitions dominated by the cold envelope in both, FIRS 2 and LkH α 234, while the (3,3) line arise in the warmer component.

In Table 9 we show the physical conditions and the molecular column densities in the warm envelope of FIRS 2 and LkH α 234. Contrary to the species tracing the cold envelope, the species tracing the warm enve-

lope present similar column densities in both targets (see Fig. 17). In fact, some species like H_2CO and C^{34}S seem to have larger column densities in LkH α 234. On the other hand, the size of the warm envelope is larger in the case of the Herbig Be star than in the case of the Class 0 YSO. Thus, the mass and size of the warm envelope remains quite constant, or even increase, during the protostellar evolution.

Although the column densities of the “warm envelope” species are not very different in the two YSOs, the origin of their emission could be different. The CH_3OH and H_2CO emission seem to be dominated by the molecular in FIRS 2. In the case of CH_3OH we have detected two components in FIRS 2. The one centered at $\sim 7 \text{ km s}^{-1}$ is clearly associated with the molecular outflow FIRS 2-out 1 and dominates the CH_3OH emission in all the transitions with $E_u < 100 \text{ K}$. We have observed only two low-energy H_2CO lines in our targets. The emission of these lines in FIRS 2 is clearly associated with the outflow FIRS 2-out 1 (see Fig. 13).

Intense CH_3OH and H_2CO lines have also been detected in LkH α 234. In this case the link between these species and the molecular outflow is not clear. In fact, these lines could arise from a warm inner envelope where the icy mantles are being evaporated releasing these species to the gas phase. Thus, although the CH_3OH and H_2CO column densities are very similar in both objects, the mechanism which removes these species from the icy mantles can be different in the Class 0 protostar FIRS 2 and the Herbig Be star LkH α 234. While shock fronts are very likely the main mechanism for the erosion of grain mantles in FIRS 2, ice evaporation could be a dominant mechanism in LkH α 234.

7.2.3. CN, HCN

The CN and HCN column densities increases from FIRS 2 to LkH α 234 by a factor of ~ 6 . This is easily understood within an evolutionary trend. Since the cold envelope has already been dispersed in LkH α 234, the UV radiation can penetrate deeper into the cloud affecting the chemistry all across the envelope in LkH α 234. The enhancement of ionization fraction (in particular, the enhancement in the C^+ abundance) in the LkH α 234 envelope could produce an enhancement in the fractional abundances of the nitrogenated chains CN and HCN relative to N_2H^+ and NH_3 .

The CN/HCN ratio has been widely used as a PDR tracer thus far. Values of the CN/HCN ratio > 1 has been considered as a prove of the existence of a photon-dominated chemistry region (see e.g. Fuente et al. 1993, 1995, 2003; Bachiller et al. 1997; Rodriguez-Franco et al. 1998). We have detected a small region in the vicinity of the Class 0 source in FIRS 2 in which the CN/HCN ratio is > 1 . This strongly suggests the existence of an incipient PDR in the inner part of this protostellar envelope. However, our limited angular resolution prevent us to discern if this PDR is associated with

the Class 0 source or with the IR companion star which is driving the outflow FIRS 2-out 2.

7.2.4. Deuterated compounds

We have observed DCO^+ and N_2D^+ in order to be able to derive the D/H ratio in the cold envelope of these stars and its possible changes during the central object evolution. Enhancements of the D/H ratio over the 10^{-5} ratio of $[\text{HD}]/[\text{H}_2]$ have been found in dark clouds and young protostars (e.g. Butner et al. 1995; Williams et al. 1998). There are two main ways of producing these enhancements. Firstly, grain surface chemistry may enhance molecular D/H ratios (Tielens 1983; Brown & Millar 1989a,b; Charnley et al. 1997). Secondly, some key gas phase reactions involving destruction of deuterated species run slower at low temperatures than the equivalent reactions with hydrogen, and this leads to molecular D/H enhancements where a cold gas phase chemistry has been active (Roberts & Millar 2000a; Roberts & Millar 2000b). Furthermore, in colder gas, depletion of heavy molecules such as CO results in an increase of $[\text{H}_2\text{D}^+]/[\text{H}_3^+]$ and molecular D/H ratios (Dalgarno & Lepp 1984; Brown & Millar 1989a; Roberts & Millar 2000a; Roberts & Millar 2000b). We have found $\text{DCO}^+/\text{H}^{13}\text{CO}^+ \sim 0.7$ in FIRS 2 and ~ 0.25 in LkH α 234. Assuming a $^{12}\text{C}/^{13}\text{C}$ isotopic ratio of 89, this would imply $\text{DCO}^+/\text{HCO}^+ \sim 0.008$ in FIRS 2 and ~ 0.003 in LkH α 234. These ratios are similar to that found in low mass Class 0 protostar IRAS+16293–2422 by van Dishoeck et al. (1995) but are lower than the values found in dark clouds (see e.g. Tiné et al. 2000). A cold gas chemistry as well as depletion of heavy molecules can explain the enhanced values $\text{DCO}^+/\text{HCO}^+$ ratio found in the young stellar object FIRS 2.

We have also observed the doubly deuterated formaldehyde D_2CO . The linewidths of the observed D_2CO lines show that this species, like the non-deuterated compound H_2CO , arise in the warm envelope. The D_2CO column densities as well as the $\text{D}_2\text{CO}/\text{H}_2\text{CO}$ ratio, are similar in LkH α 234 than in FIRS 2. This suggests that the deuterium fractionation remains constant (or even increase, see Table 9) in the warm envelope during the protostellar evolution. Thus, the evolution of the deuterium fractionation is different in the cold and warm part of the envelope. Grain-surface chemistry may enhanced the deuterium fractionation in the warm envelope where molecular evaporation is very likely the main chemical phenomenon, while the cold gas chemistry and depletion could determine the evolution of the deuterium fractionation in the cold envelope.

The deuterium fractionation has been proposed as a chemical clock in YSOs. Our data confirms that the deuterium fractionation changes significantly during the protostellar evolution and consequently, can be used as a chemical clock. However, these changes are different in the cold and in the warm part of the envelope, and the

Table 9. Beam averaged column densities

| | NGC 7129 – FIRS 2 | LkH α 234 |
|---|-------------------------------|-----------------------|
| Age | $\gtrsim 3000$ yr | $\sim 10^5$ yr |
| $n(\text{cm}^{-3})$ | $5 \cdot 10^5 - 3 \cdot 10^6$ | $2 \cdot 10^5$ |
| Cold envelope | | |
| T_k | 13 K | 28 K |
| Ω_s | $\sim 21''$ | $\sim 8''$ |
| NH_3 | $4.9 \cdot 10^{14}$ | $4.0 \cdot 10^{13}$ |
| N_2H^+ | $3.8 \cdot 10^{13}$ | $1.0 \cdot 10^{13}$ |
| H^{13}CO^+ | $2.2 \cdot 10^{12}$ | $1.7 \cdot 10^{12}$ |
| DCO^+ | $1.8 \cdot 10^{12}$ | $4.2 \cdot 10^{11}$ |
| N_2D^+ | $5.4 \cdot 10^{11}$ | $< 2.3 \cdot 10^{11}$ |
| $\text{N}_2\text{H}^+/\text{H}^{13}\text{CO}^+$ | 17 | 6 |
| $\text{NH}_3/\text{N}_2\text{H}^+$ | $13 - 33^b$ | 10 |
| $\text{DCO}^+/\text{H}^{13}\text{CO}^+$ | 0.7 | 0.2 |
| $\text{N}_2\text{D}^+/\text{N}_2\text{H}^+$ | 0.014 | < 0.02 |
| Warm envelope | | |
| T_k | > 50 K | > 100 K |
| Ω_s | $\sim 9''$ | $\sim 14''$ |
| C^{34}S | $1.5 \cdot 10^{12}$ | $1.7 \cdot 10^{12}$ |
| CH_3OH | $9.8 \cdot 10^{14}$ | $5.4 \cdot 10^{14}$ |
| CH_3CN | $3.6 \cdot 10^{12}$ | $> 2.0 \cdot 10^{12}$ |
| H_2CO | $7.0 \cdot 10^{13}$ | $8.0 \cdot 10^{13}$ |
| H_2^{13}CO | $2.3 \cdot 10^{12}$ | $2.4 \cdot 10^{12}$ |
| D_2CO | $2.0 \cdot 10^{12}$ | $3.7 \cdot 10^{12}$ |
| $\text{D}_2\text{CO}/\text{H}_2\text{CO}$ | 0.03 | 0.05 |
| PDR | | |
| CN | $4.8 \cdot 10^{13}$ | $6.1 \cdot 10^{13}$ |
| HCN | $1.6 \cdot 10^{13}$ | $2.1 \cdot 10^{13}$ |
| Outflow | | |
| SiO | $2.8 \cdot 10^{12}$ | $2.0 \cdot 10^{11}$ |

^b Assuming beam filling factor ~ 1 and a source size of $21''$ for the NH_3 emitting region.

Table 10. Chemical diagnostics for YSO evolution

| | NGC 7129 – FIRS 2 | LkH α 234 |
|------------------------------------|-------------------|------------------|
| $\text{SiO}/\text{C}^{34}\text{S}$ | ~ 2 | ~ 0.1 |
| $\text{CN}/\text{N}_2\text{H}^+$ | ~ 1 | ~ 6 |
| $\text{HCN}/\text{N}_2\text{H}^+$ | ~ 0.4 | ~ 2 |
| $\text{DCO}^+/\text{HCO}^+$ | ~ 0.008 | ~ 0.002 |
| $\text{D}_2\text{CO}/\text{DCO}^+$ | ~ 1 | ~ 10 |

measured D/H ratio is very dependent on the molecular compounds used to determine it.

8. Summary and Conclusions: Chemical-clocks in intermediate-mass YSOs

We have carried out a molecular survey towards the IM YSOs FIRS 2 and LkH α 234. Our survey confirms that protostellar envelopes are very complex objects composed by several components characterized by different physical and chemical properties:

1. A cold envelope observationally characterized by narrow lines ($\Delta v \sim 1 \text{ km s}^{-1}$) and low kinetic temperatures

($T_k < 50$ K). This component is well traced by the species $\text{NH}_3, \text{N}_2\text{H}^+, \text{H}^{13}\text{CO}^+, \text{DCO}^+$ and N_2D^+ .

2. A warm envelope observationally characterized by large linewidths ($\Delta v > 3 \text{ km s}^{-1}$) and kinetic temperatures ($T_k > 50$ K). The low energy transitions of $\text{CS}, \text{C}^{34}\text{S}, \text{CH}_3\text{OH}$, and H_2CO arise in this warm component.
3. A hot core characterized by high densities ($n > 10^6 \text{ cm}^{-3}$) and a high kinetic temperature ($T_k > 100$ K). The symmetric rotor CH_3CN seems to be the best tracer of this hot component.
4. In addition to these envelope components, energetic outflows are associated with very YSOs. In addition to CO and its isotopes, the SiO emission is very likely the best tracer of the outflow component for very young stellar objects.

Once, we have used chemistry to determine the physical structure of the YSOs, FIRS 2 and LkH α 234, we can determine the evolution of the protostellar envelopes of IM stars during the protostellar phase. FIRS 2 is an IM Class 0 objects while LkH α 234 is a very young (and still deeply embedded) HBe star. As expected, different physical conditions and chemistry are found in these objects. The Class 0 IM is a cold object ($T_k \sim 13$ K) in which molecular depletion is still important. We have no evidence of a change in the N_2H^+ abundance between both objects. The decrease in the N_2H^+ column density observed in Fig. 17 is the consequence of the disruption of the cold envelope during the stellar evolution. However, we have found evidences for H^{13}CO^+ depletion in FIRS 2. Molecules like CH_3OH and H_2CO are expected to trace mainly the warm region in which grain mantles have been evaporated. The column densities of these molecules remain constant (or increase) from the Class 0 IM to the more evolved HBe star, suggesting that the abundances of these molecules and/or the mass of the warm gas increases with the protostellar evolution. The detection of CH_3CN and the high temperature derived from it ($T_k \sim 63$ K) shows that a hot core has developed in the Class 0 protostar FIRS 2. Thus, our results suggest an evolutionary sequence in which as the protostar evolves to become a visible star, the total column density of gas is decreasing while the amount of warm gas remains quite constant or slightly increase. These physical and chemical changes imply important changes in the beam averaged column densities during the protostellar evolution.

Based on our observational study of FIRS 2 and LkH α 234, we propose some abundance ratios that can be used as chemical clocks in YSOs. These ratios are defined to be useful tools to discern between different evolutionary stages of YSOs, but do not correspond to the actual abundance ratios in any of the envelope components. They have been calculated with beam averaged column densities and, as largely discussed in this paper, are the consequence of a complex physical and chemical evolution in the whole envelope.

In Table 10 we list the proposed chemical clocks. We find the maximum variation between the Class 0 and the HBe object when comparing the SiO/C³⁴S ratio. This ratio decreases by a factor of ~ 20 between these two objects. This decrease is the consequence of the decay of the bipolar outflow phenomenon during the protostellar evolution. This ratio is specially useful to determine the evolutionary stage of the youngest objects which are associated with the most energetic bipolar outflows. The nitrogen chemistry is also useful to determine the evolutionary stage of YSOs. The CN/N₂H⁺ and HCN/N₂H⁺ ratios are larger by a factor of ~ 6 in the HBe star than in the Class 0 object. As commented above this is mainly due to the fact that the LkH α 234 envelope is thinner and warmer than that of the FIRS 2. These ratios would probably be more useful to differentiate between objects in the late protostellar evolution when the protostellar envelope becomes optically thinner. Finally, the deuterated species could also be a good indicator of the protostellar evolution. The DCO⁺/HCO⁺ ratio decreases by a factor ~ 4 due to the warmer envelope in LkH α 234. However, we can have a different behavior in the deuterated species whose emission arise in the warm envelope component. This is the case of the doubly deuterated compound D₂CO. We obtain the largest contrast in the abundance ratio if we compare the D₂CO and DCO⁺ abundances. The D₂CO/DCO⁺ ratio increases by a factor of 10 from the Class 0 to the Herbig Be star. However, we should be cautious using this ratio because we are comparing species arising in different regions of the envelope.

Acknowledgements. We are grateful to the MPIFR and IRAM staff in Pico de Veleta for their support during the observations. This work has been partially supported by the Spanish DGICYT under grant AYA2003-07584 and Spanish DGI/SEPCT under grant ESP2003-04957. J.R.R. acknowledges the financial support from AYA2003-06473.

References

- André, P., Ward-Thompson, D., & Barsony, M. 2000, *Protostars and Planets IV*, 59
- Bachiller, R., Guilloteau, S., & Kahane, C. 1987, *A&A*, 173, 324
- Bachiller, R., Martin-Pintado, J., & Fuente, A. 1991, *A&A*, 243, L21
- Bachiller, R. 1996, *IAU Symp. 178: Molecules in Astrophysics: Probes & Processes*, 178, 103
- Bachiller, R., Fuente, A., Bujarrabal, V., Colomer, F., Loup, C., Omont, A., & de Jong, T. 1997, *A&A*, 319, 235
- Bachiller, R., Pérez Gutiérrez, M., Kumar, M. S. N., & Tafalla, M. 2001, *A&A*, 372, 899
- Bottinelli, S., Ceccarelli, C., Lefloch, B., et al., 2004, *ApJL* submitted
- Brown, P. D., Charnley, S. B., & Millar, T. J. 1988, *MNRAS*, 231, 409
- Brown, P. D. & Millar, T. J. 1989a, *MNRAS*, 240, 25P
- Brown, P. D. & Millar, T. J. 1989b, *MNRAS*, 237, 661
- Butner, H. M., Lada, E. A., & Loren, R. B. 1995, *ApJ*, 448, 207
- Caselli, P., Hasegawa, T. I., & Herbst, E. 1993, *ApJ*, 408, 548
- Caselli, P., Walmsley, C. M., Tafalla, M., Dore, L., & Myers, P. C. 1999, *ApJ Let*, 523, L165
- Caselli, P., Walmsley, C. M., Zucconi, A., Tafalla, M., Dore, L., & Myers, P. C. 2002, *ApJ*,
- Cazaux, S., Tielens, A. G. G. M., Ceccarelli, C., Castets, A., Wakelam, V., Caux, E., Parise, B., & Teyssier, D. 2003, *ApJL* 593, L51
- Charnley, S. B., Tielens, A. G. G. M., & Millar, T. J. 1992, *ApJ Let*, 399, L71
- Charnley, S. B., Tielens, A. G. G. M., & Rodgers, S. D. 1997, *ApJ Let*, 482, L203
- Codella, C., Bachiller, R., & Reipurth, B. 1999, *A&A*, 343, 585
- Dalgarno, A. & Lepp, S. 1984, *ApJ Let*, 287, L47
- Danby, G., Flower, D. R., Valiron, P., Schilke, P., & Walmsley, C. M. 1988, *MNRAS* 235, 229
- Eiroa C., Palacios J., Casali M. M., 1998, *A&A* 335, 243
- Flower, D. R., Pineau des Forêts, G., Field, D., & May, P. W. 1996, *MNRAS*, 280, 447
- Fuente, A., Martin-Pintado, J., Cernicharo, J., & Bachiller, R. 1993, *A&A*, 276, 473
- Fuente, A., Martin-Pintado, J., & Gaume, R. 1995, *ApJ Let*, 442, L33
- Fuente, A., Martin-Pintado, J., Bachiller, R., Neri, R., & Palla, F. 1998, *A&A* 334, 253
- Fuente, A., Neri, R., Martin-Pintado, J., Bachiller, R., Rodriguez-Franco, A., & Palla, F. 2001, *A&A*, 366, 873
- Fuente, A., Martin-Pintado, J., Bachiller, R., Rodriguez-Franco, A., & Palla, F. 2002, *A&A* 387, 977
- Fuente, A., Rodriguez-Franco, A., Garcia-Burillo, S., Martin-Pintado, J., & Black, J. H. 2003, *A&A*, 406, 899
- Garcia-Burillo, S., Martin-Pintado, J., Fuente, A., & Neri, R. 2001, *ApJ Let*, 563, L27
- Garcia-Burillo, S., Martin-Pintado, J., Fuente, A., & Neri, R. 2000, *A&A*, 355, 499
- Green, S. & Chapman, S. 1978, *ApJS*, 37, 169
- Gueth, F., Guilloteau, S., & Bachiller, R. 1996, *A&A*, 307, 891
- Lee J.-E., Evans N.J., & Shirley Y.L., 2003, *ApJ* 583, 789
- Jørgensen, J. K., Hogerheijde, M. R., van Dishoeck, E. F., Blake, G. A., & Schöier, F. L. 2004a, *A&A*, 413, 993
- Jørgensen, J. K., Schöier, F. L., & van Dishoeck, E. F. 2004b, *A&A*, 416, 603
- Maret, S., et al. 2004, *A&A*, 416, 577
- Martin-Pintado, J., Bachiller, R., & Fuente, A. 1992, *A&A*, 254, 315
- Nomura, H. & Millar, T. J. 2004, *A&A*, 414, 409
- Pickett H.M., Poynter R.L., Cohen E.A., Delitsky M.L., Pearson J.C., Muller H.S.P., 1998, *J. Quant. Spectrosc. & Rad. Transfer* 60, 883
- Ray, T.P., Poetzel, R., Solf, J., & Mundt, R., 1990, *ApJL*, 357, L45
- Roberts, H. & Millar, T. J. 2000a, *A&A*, 361, 388
- Roberts, H. & Millar, T. J. 2000b, *A&A*, 364, 780
- Rodgers, S. D. & Charnley, S. B. 2003, *ApJ*, 585, 355
- Rodriguez-Franco, A., Martin-Pintado, J., & Fuente, A. 1998, *A&A*, 329, 1097
- Schilke, P., Pineau des Forêts, G., Walmsley, C. M., & Martin-Pintado, J. 2001, *A&A*, 372, 291
- Tafalla, M., Myers, P. C., Caselli, P., Walmsley, C. M., & Comito, C. 2002, *ApJ*, 569, 815
- Tafalla, M., Myers, P. C., Caselli, P., & Walmsley, C. M. 2004, *A&A*, 416, 191
- Testi, L., Palla, F., & Natta, A. 1999, *A&A*, 342, 515

- Tielens, A. G. G. M. 1983, *A&A*, 119, 177
 Tiné, S., Roueff, E., Falgarone, E., Gerin, M., & Pineau des Forêts, G. 2000, *A&A*, 356, 1039
 van Dishoeck, E. F., Blake, G. A., Jansen, D. J., & Groesbeck, T. D. 1995, *ApJ*, 447, 760
 Van der Tak, F. F. S., van Dishoeck, E. F., & Caselli, P. 2000, *A&A*, 361, 327
 Viti, S., Collings M.P., Dever J.W., McCoustra M.R.S., Williams D.A., in press ([astro-ph0406054](#))
 Williams J.P., Bergin E.A., Caselli P., Myers P.C., Plume R., 1998, *ApJ* 503, 689
 Wolfire M.G., McKee C.F., Hollenbach D., Tielens A.G.G.M., 2003, *ApJ* 587, 278

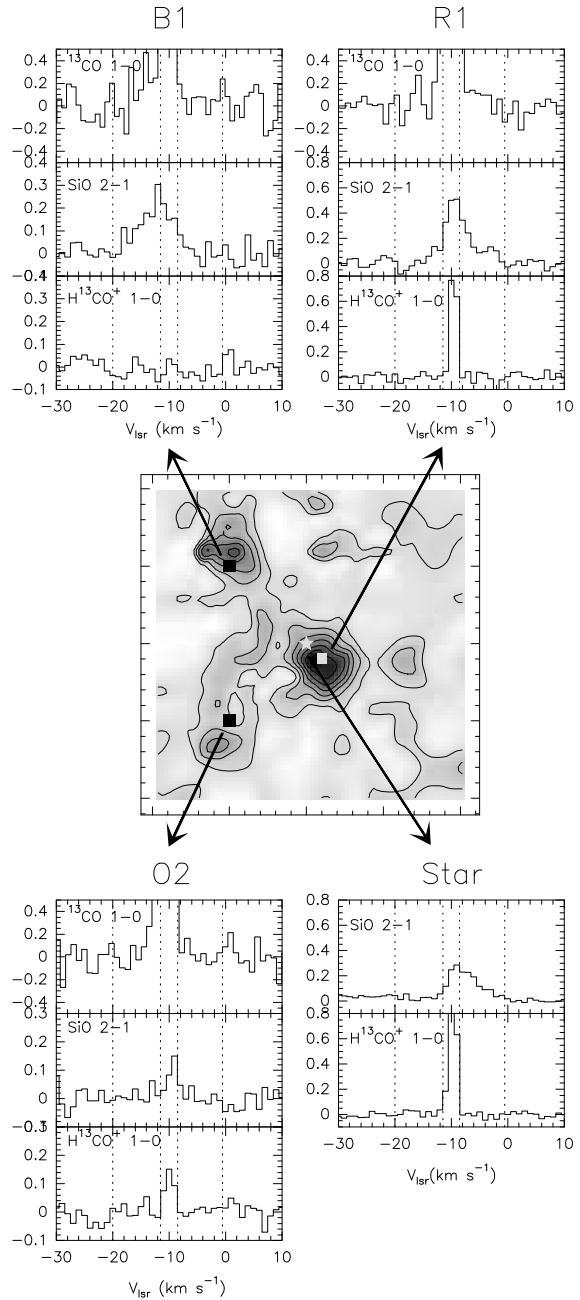


Fig. 8. In the central panel we show the integrated line intensity map of the SiO $J=2\rightarrow 1$ line toward FIRS 2. Contour levels are from 0.25 K km s^{-1} to 4 K km s^{-1} by steps of 0.5 K km s^{-1} . Surrounding the central panel, we show the observed spectra of the ^{13}CO $1\rightarrow 0$, SiO $2\rightarrow 1$ and H^{13}CO^+ $1\rightarrow 0$ lines towards selected positions of outflows FIRS 2-out 1 (top panels) and FIRS 2-out 2 (bottom panels). The intensity scale in the spectra is main brightness temperature.

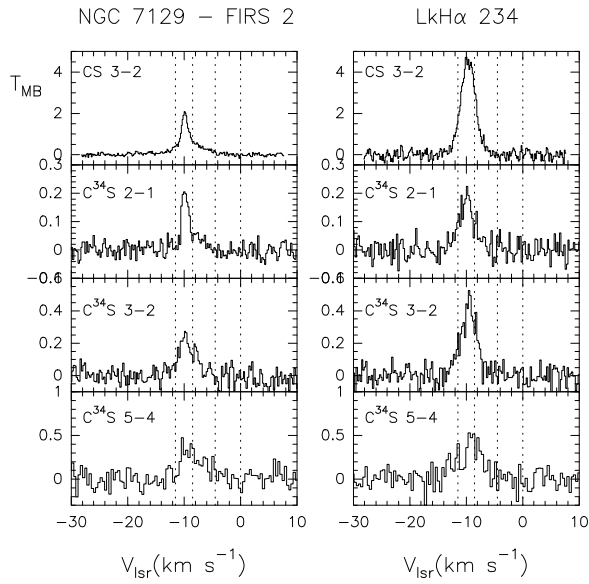


Fig. 9. Observed CS and $C^{34}S$ spectra towards the (0,0) position in NGC 7129 – FIRS 2 and LkH α 234.

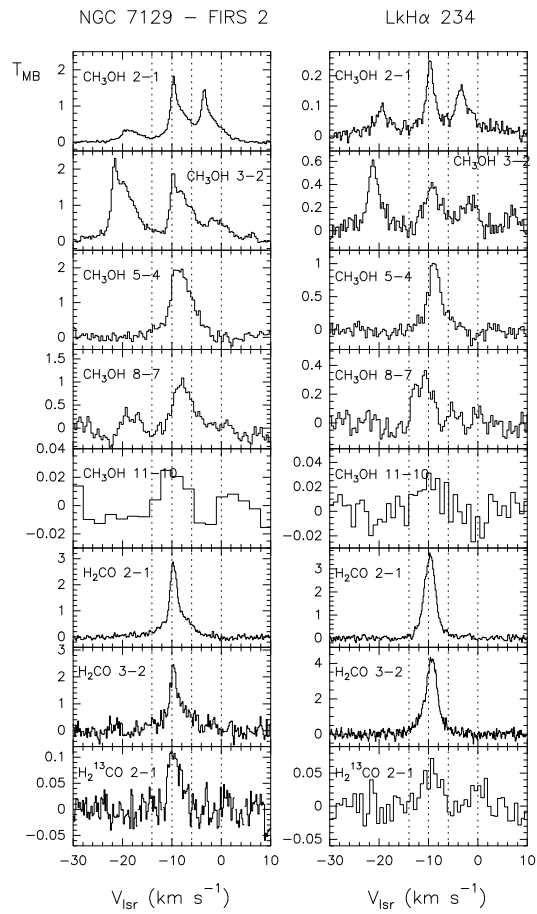


Fig. 10. Observed spectra of CH_3OH and H_2CO lines towards the (0,0) position in NGC 7129 – FIRS 2 and LkH α 234..

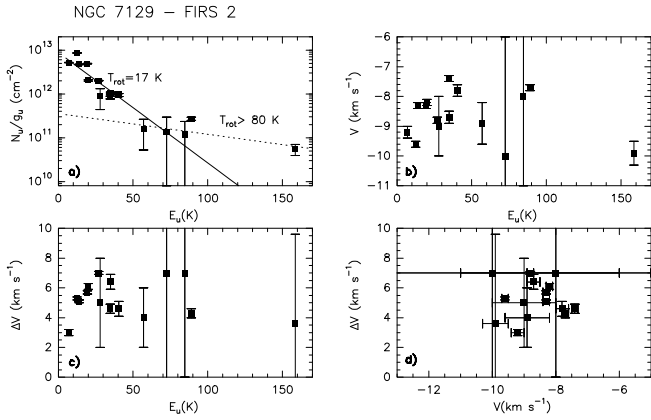


Fig. 11. The (a) panel shows the rotational diagram for CH_3OH in the (0,0) position of NGC 7129 – FIRS 2. We have degraded the angular resolution of the 1.3mm maps (the 5→4 and 8→7 methanol lines) in order to have the angular resolution of the 3mm maps (lines 2→1 and 11→10 lines). Two rotation temperatures ($T_{rot}=17$ K and $T_{rot}>80$ K) are required to fit the data). In the (b) and (c) panels we plot the line velocities and linewidths, V and ΔV , of the CH_3OH lines as given by the gaussian fits shown in Table 3 versus the upper state energy of the observed transition (E_u). Finally, the (d) panel shows V versus ΔV for the CH_3OH lines. This panel clearly shows the existence of two velocity components, one at ~ -10 km s^{-1} and the other at ~ -6 km s^{-1} in this position.

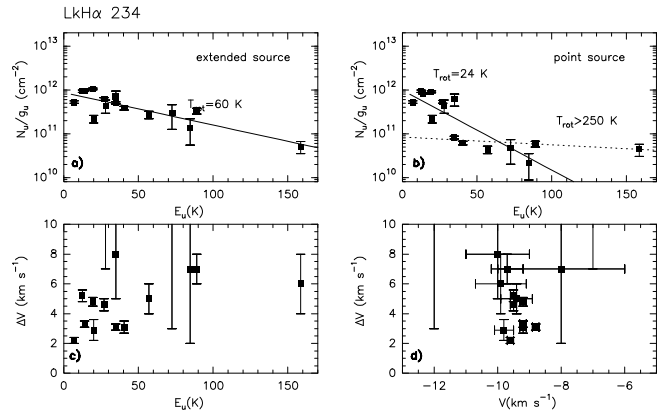


Fig. 12. The top panels show the rotational diagram for CH_3OH in LkH α 234 in the two limit cases assumed in the paper, panel (a) corresponds to a beam filling factor ~ 1 and panel (b) corresponds to a point source. In the bottom panels we plot the linewidths, Δv , derived from the Gaussian fits versus the upper energy state of the transition, E_u , and the central velocity, V , for all the lines. In the case of LkH α 234 we have only one velocity component.

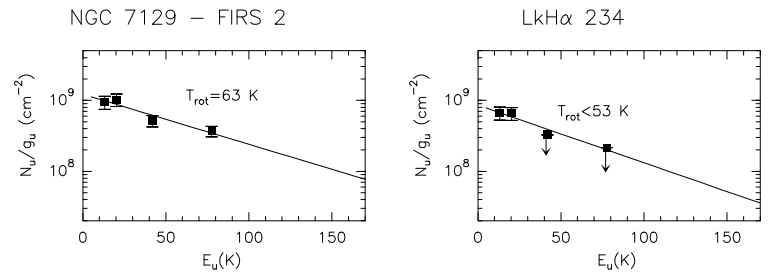


Fig. 14. Rotational diagram of CH_3CN in the (0,0) position of FIRS 2 and LkH α 234.

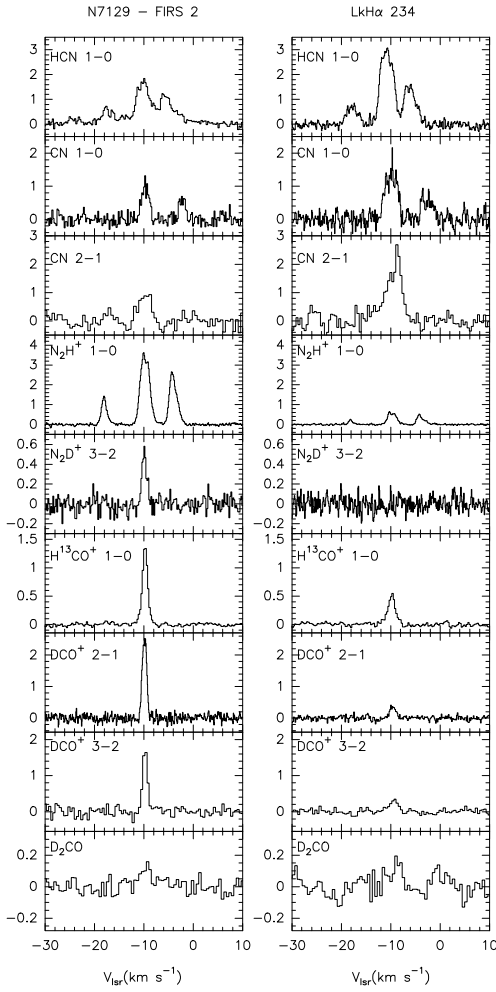


Fig. 15. Observed spectra towards the (0,0) position in LkH α 234 and NGC 7129 – FIRS 2. The warming of the gas during the protostellar evolution, produces significant chemical changes specially in the cold component.

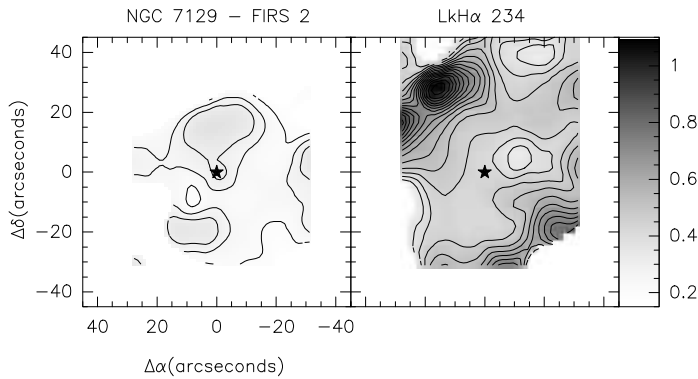


Fig. 16. CN 1 \rightarrow 0 / HCN 1 \rightarrow 0 integrated intensity ratio in NGC 7129 – FIRS 2 (left) and LkH α 234 (right). Contour levels are 0.10 to 0.35 by 0.05 in NGC 7129 – FIRS 2 and 0.35 to 1.1 by 0.05 in LkH α 234.